UNCLASSIFIED

AD NUMBER

AD142088

NEW LIMITATION CHANGE

TO

Approved for public release, distribution unlimited

FROM

Distribution authorized to U.S. Gov't. agencies and their contractors; Administrative/Operational Use; Nov 1957. Other requests shall be referred to Wright Air Development Center, Wright-Patterson AFB, OH 45433.

AUTHORITY

Air Force Flight Dynamics Lab ltr 10 May 1976

THIS PAGE IS UNCLASSIFIED

UNCLASSIFIED

AD 142088

DEFENSE DOCUMENTATION CENTER

FOR

SCIENTIFIC AND TECHNICAL INFORMATION

CAMERON STATION ALEXANDRIA, VIRGINIA

CLASSIFICATION CHANGED
TO UNCLASSIFIED
FROM CONFIDENTIAL
PER AUTHORITY LISTED IN

Bul. no. 66-20 15 Oct. 1966

UNCLASSIFIED

NOTICE: When government or other drawings, specifications or other data are used for any purpose other than in connection with a definitely related government procurement operation, the U. S. Government thereby incurs no responsibility, nor any obligation whatsoever; and the fact that the Government may have formulated, furnished, or in any way supplied the said drawings, specifications, or other data is not to be regarded by implication or otherwise as in any manner licensing the holder or any other person or corporation, or conveying any rights or permission to manufacture, use or sell any patented invention that may in any way be related thereto.

CONFIDENTIAL

AD No. 142088
ASTIA FILE COPY

2.5

WADC TECHNICAL REPORT 56-285
ASTIA DOCUMENT NO. AD-142088

(UNCLASSIFIED TITLE)

FLUTTER MODEL TESTS OF A SWEPT-BACK, ALL-MOVING HORIZONTAL TAIL AT SUPERSONIC SPEEDS

Gifford W. Asher
John [illegible] Martuccelli
Warren H. Weatherill

MASSACHUSETTS INSTITUTE OF TECHNOLOGY

NOVEMBER 1957

FC

FEB 21 1958

WRIGHT AIR DEVELOPMENT CENTER

56 WCLS 10322-26

58 [illegible] 309

AF-WP-B-O 14 JAN 58

CONFIDENTIAL

CONFIDENTIAL

WADC TECHNICAL REPORT 56-285

ASTIA DOCUMENT NO. AD-142088

(UNCLASSIFIED TITLE)

FLUTTER MODEL TESTS OF A SWEPT-BACK, ALL-MOVING HORIZONTAL TAIL AT SUPERSONIC SPEEDS

Gifford W. Asher

John R. Martuccelli

Warren H. Weatherill

Massachusetts Institute of Technology

NOVEMBER 1957

Aircraft Laboratory

Contract AF 33(616)-2751

Project No. 1370

Wright Air Development Command

Air Research and Development Command

United States Air Force

Wright-Patterson Air Force Base, Ohio

56 WCLS 10322

58 09

CONFIDENTIAL

FOREWORD

This report, which presents the experimental and theoretical results of a program conducted to investigate the supersonic flutter characteristics of a swept-back all-movable surface, was prepared by the Aeroelastic and Structures Research Laboratory, Massachusetts Institute of Technology, Cambridge 39, Massachusetts for the Aircraft Laboratory, Wright Air Development Center, Wright-Patterson Air Force Base, Ohio. The work was performed at MIT under the direction of Professor R. L. Halfman, and the project was supervised by Mr. G. W. Asher. The research and development work was accomplished under Air Force Contract No. AF 33(616)-2751, Project No. 1370 (UNCLASSIFIED TITLE) "Aeroelasticity, Vibration and Noise," and Task No. 13479, (UNCLASSIFIED TITLE) "Investigation of Flutter Characteristics of All-Movable Tails," with Mr. Niles R. Hoffman of the Dynamics Branch, Aircraft Laboratory, WADC as task engineer. This research was started in January 1955 and completed in September 1956. Additional supersonic flutter testing of swept all-movable stabilizers may be performed at a later date to obtain further information.

The authors are indebted to Mr. O. Wallin and Mr. C. Fall for their help in building the models and in keeping the experimental equipment in good order, and to Mr. G. M. Falla for his help in making the high speed photographs. The authors are also indebted to Messrs. A. Heller, Jr., J. R. Friery and H. Moser for their help in preparing the necessary calculations, tables, and figures for this report.

Portions of this document are classified CONFIDENTIAL since the data revealed can be employed to establish design criteria for the prevention of flutter of swept-back all-movable tails of aircraft in the supersonic speed range.

ABSTRACT

This report describes the flutter testing at supersonic speeds of a series of swept-back all-moving stabilizers. An attempt was made to define the flutter boundaries, for one location of the pitching axis, over the Mach number range of 1.3 to 2.1, by testing at a number of different levels of stabilizer stiffness, and at a number of different pitching frequencies.

The results indicate that large increases in the region of instability can occur due to the introduction of the pitching degrees of freedom. The test results follow the trends of theoretical calculations, but the quantitative correlation between the theoretical and the experimental results is only fair.

PUBLICATION REVIEW

This report has been reviewed and is approved.

FOR THE COMMANDER:

J H Harrington
for RANDALL D. KEATOR
Colonel, USAF
Chief, Aircraft Laboratory

TABLE OF CONTENTS

LIST OF ILLUSTRATIONS

LIST OF ILLUSTRATIONS (Cont.)

List of Tables

LIST OF SYMBOLS

NOTE

All quantities marked with * are measured in an unswept reference system except when appearing with subscript Ω. They are then being referred to a reference system swept with the elastic axis (see Fig. 8 for unswept x, y and swept x_Ω, y_Ω reference systems).

a	*Location of elastic axis in semichords aft of stabilizer midchord
a	Speed of sound (ft/sec), $a = 49.1\sqrt{T}$
AR	Panel aspect ratio
b	*Semichord of stabilizer (ft)
c	*Chord of stabilizer (ft)
C_ϕ	Flexibility influence coefficient of pitching mechanism (rad/ft-lb)
d	*Distance between pitch axis and elastic axis at the root, positive aft (ft)
ea	Elastic axis or shear center position (% chord)
E	Modulus of elasticity in bending
EI	*Bending stiffness
f	Frequency (cps)
F	Assumed mode shape for calculation
g	Structural damping coefficient (ref. 10)
G	Modulus of elasticity in torsion
GJ	*Torsional stiffness
h	Vertical displacement of stabilizer elastic axis (ft)
$\bar{h}_1, \bar{h}_2$	See Appendix I, Eq. (1)
I_α	*Mass moment of inertia of stabilizer per unit span about the elastic axis (slug-ft^2)
I_ϕ	Mass moment of inertia of rigid stabilizer about pitch axis (slug-ft^2)
k	*Reduced frequency, $b\omega/V$; ($k = k_\Omega$)
ℓ	*Semi span of model (ft)
L, M	Aerodynamic coefficients (see Appendix I)
LE	Leading edge
m	*Mass of stabilizer per unit span (slug/ft)
M	*Mach number
r_α	*Section radius of gyration ($r_\alpha^2 = I_\alpha/mb^2$) in semichords
S_α	*Static mass unbalance per unit span about elastic axis (slug-ft/ft)

t	Time (secs)
T	Absolute temperature (°R)
TE	Trailing edge
V	*Velocity (ft/sec)
x, y, z	*Coordinate distances (shown in Appendix I, Fig. 8)
x_α	*Distance section center of gravity of the stabilizer lies aft of elastic axis in semichords
α	*Torsional deflection of the stabilizer, positive nose up (radians)
$\bar{\alpha}$	*See Appendix I, Eq. (1)
η	*Nondimensional spanwise coordinate, $\eta = y/\ell$
λ	Taper ratio, tip chord/root chord
Ω	Angle of sweep of elastic axis, positive for sweep-back, (degrees)
μ	*Relative density, $\mu = m/\pi\rho\ b^2$ (constant along the span)
ρ	Air density (slug/ft^3)
ϕ	Rigid body pitching about pitch axis, positive nose up
$\bar{\phi}$	See Appendix I, Eq. (1)
ω	Frequency (rad/sec)
Z	Flutter parameter $(\omega_{\alpha_1}/\omega_f)^2$, Eq. (23)
Z_a	Deflection of the mean surface of the stabilizer (ft)

SUBSCRIPTS

f	Conditions at start of flutter
h_1, h_2	First and second uncoupled bending modes of the stabilizer
h_N	First measured cantilever or "pitch locked" bending mode of the stabilizer (Nominal first bending frequency)
L	Pertaining to pitch-locked-out condition
M	Experimentally determined parameter
0	Parameter evaluated at the root of the stabilizer ($y = 0$)
0.75	Parameter evaluated at the 75% span station of the stabilizer
r	Reference station for theoretical calculations (75% span station of the stabilizer)
T	Parameter evaluated at tip of stabilizer ($y = \ell$)
α_1	First uncoupled torsional mode of the stabilizer
α_N	First measured cantilever, or "pitch locked," torsional mode of the stabilizer (Nominal first torsional frequency)
Ω	Parameter measured in reference system swept with the elastic axis
ϕ	Rigid pitch degree of freedom
1, 2	First and second measured coupled modes
$(1/4)c$	Quarter chord

SECTION I

INTRODUCTION

This report covers the experimental flutter tests and associated theoretical calculations made on a swept, all-moving horizontal stabilizer at supersonic speeds. The configuration tested is becoming a common one for high speed aircraft and missiles.

At present, the methods of theoretical supersonic flutter analysis using two-dimensional aerodynamic forces derived from linearized theory do not appear adequate to predict the absolute levels of the flutter boundaries. Reference 3 shows that even for the simple cantilever straight wings analyzed in that report such analyses give results that are conservative in one Mach number range and unconservative in another. It may be suspected that the poor correlation between theoretical and test results shown in Ref. 3 arises from the use of two-dimensional aerodynamic forces on a three-dimensional lifting surface, and so the use of more powerful methods of analysis, such as the aerodynamic influence coefficient methods of Refs. 5 and 6, may improve the correlation. However, correlations between theoretical and experimental results, where the theoretical calculations have been based on three-dimensional aerodynamic forces, are not common in the supersonic regime. Until such correlations have been made, it is not certain that the added labor of the influence coefficient methods will be worth while in terms of improved results. The designer will probably rely on the simpler two-dimensional calculation to supply a description of the trends to be expected when various parameters are changed, and will probably depend for some time on what experimental data is available or can be obtained to define the absolute levels of the flutter boundaries.

The present program is intended to define experimentally the level of the flutter boundaries for an all-moving, swept horizontal stabilizer. The cantilever, or "pitch locked," boundary is defined by tests of the cantilever configuration of the model shown in Fig. 14a, and through the use of data from previous flutter tests. Various levels of wing and pitching restraint stiffness are then combined in an attempt to define the effect of the pitching degree of

---

Manuscript released by the authors September 1957 for publication as a WADC Technical Report.

freedom on the flutter boundaries, over the Mach number range 1.3 to 2.0. The results are discussed in Section II of this report, and a complete compilation of the experimental data is found in Appendix II.

Along with the experimental program, a large number of theoretical calculations have been made on the basis of two-dimensional aerodynamic coefficients, both supersonic and incompressible. The major effort was expended on three-degree-of-freedom calculations employing assumed wing bending and wing torsion structural modes and a rigid pitching mode. Four-degree-of-freedom calculations were also made which included an assumed second bending mode as well as the previously mentioned modes. The results of the calculations are discussed in Section II, and the equations used for setting up the calculations are described in Appendix I.

SECTION II

DISCUSSION OF RESULTS

1 Discussion of Theoretical Results

A considerable number of calculations were made during the course of the program for the swept stabilizer models to determine, if possible, what trends might be expected in the flutter boundaries for models of various stiffness levels and varying pitch frequencies. The calculations used the velocity component method of Ref. 8 with two dimensional aerodynamic coefficients. The model for calculation of the aerodynamic integrals was assumed to be untapered in order to avoid variations of reduced frequency, $k = b\omega_f/v$, along the span, but the mass and stiffness parameters were assumed to vary in the same manner as the experimental model. A description of the calculations is found in Appendix I.

Most of the theoretical effort was expended on three-degree-of-freedom calculations employing supersonic aerodynamic coefficients. The three degrees of freedom used for this analysis were wing first bending (parabolic), wing first torsion (linear), and rigid pitch about the rotation axis. The results of these calculations are given in Fig. 1 for various values of the pitching to torsion frequency ratio $(\omega_\phi/\omega_{\alpha_1})^2$ and pitching to first bending frequency ratio $(\omega_\phi/\omega_{h_1})^2$. In all of the calculations $(\omega_{h_1}/\omega_{\alpha_1}) = 0.25$, where ω_{h_1}, ω_{α_1}, and ω_ϕ refer to the frequencies in the assumed uncoupled modes. Note that the reference semichord for the calculations, b_r, is that of the 75 % span station, $b_{0.75}$. The reference axes for measuring the semichord as well as other similar quantities are aligned with the stream unless a subscript Ω is used. In that case the reference axes are swept with the elastic axis (See Fig. 8). Many of the parameters, such as μ, are constant along the span.

Perhaps the most interesting feature shown in Fig. 1 is the sharp increase in the region of instability that occurs below Mach numbers of about 1.8 for a value of $(\omega_\phi/\omega_{\alpha_1})^2 = 0.20$. For this value of $(\omega_\phi/\omega_{\alpha_1})^2$, the boundary actually crosses the $M = 1.7$ line three times giving the shape shown. As noted in Appendix I, the four-degree-of-freedom calculations indicated that this sharp drop or "bucket" in the boundary probably occurs because of a change in the mode of

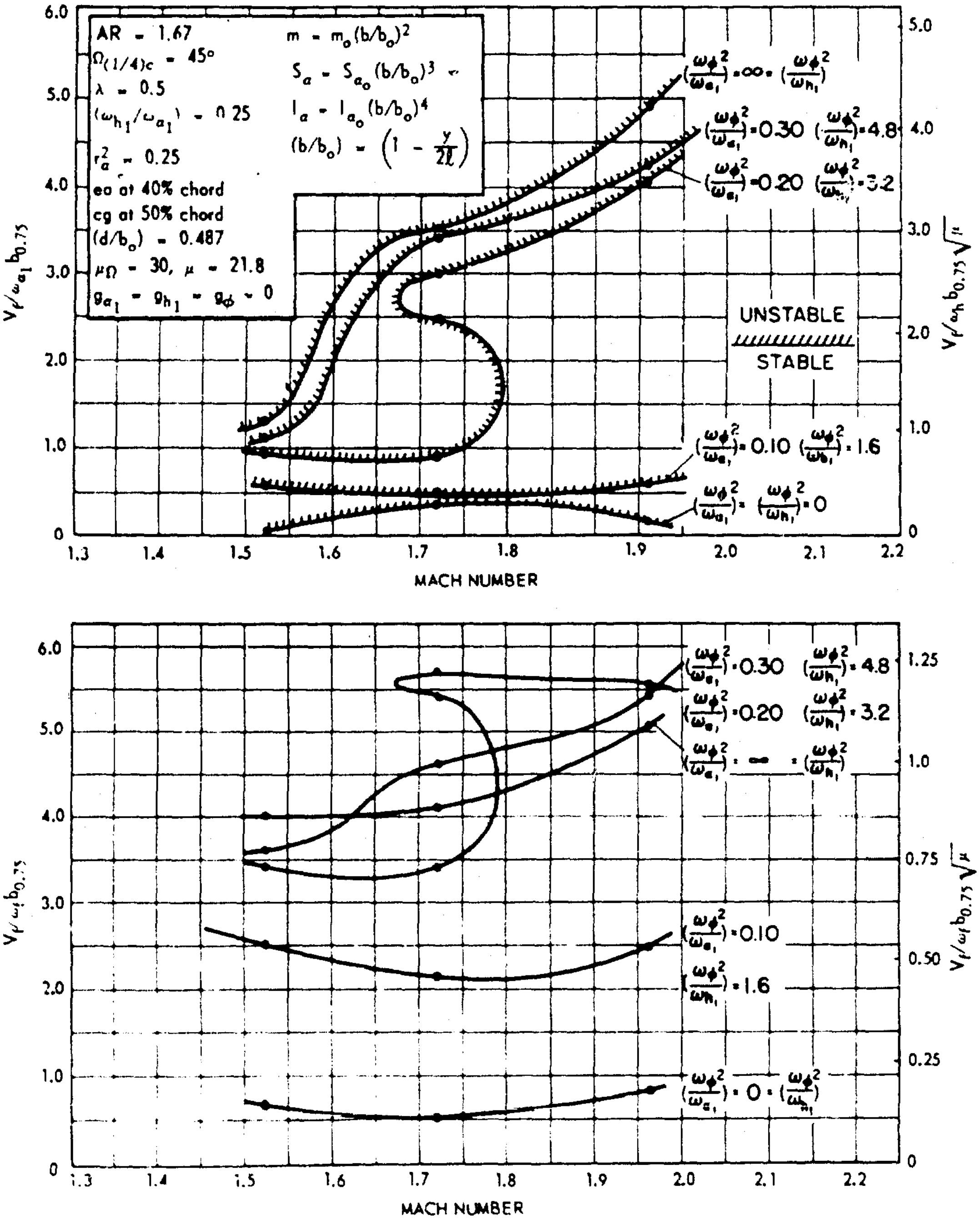

Fig. 1. Flutter parameters $V_f/\omega_{\alpha_1} b_{0.75}$ and $V_f/\omega_f b_{0.75}$ versus Mach number from three-degree-of-freedom supersonic calculations.

flutter. Figure 13 of Appendix I shows that the "bucket" may be very much affected by the level of structural damping, g, to the extent that for g about 0.6 the boundary for $(\omega_\phi/\omega_{\alpha_1})^2 = 0.20$ may follow smoothly the trend established by the cantilever, or "locked" case $(\omega_\phi/\omega_{\alpha_1})^2 = \infty$.

For high pitch frequencies the velocity - Mach number trend is similar to the locked pitch case with only a moderate lowering of the flutter velocity. For low pitch frequencies the velocity - Mach number trend appears to be nearly a constant equivalent airspeed $(\sqrt{\sigma}\,V = \text{constant})$ through a wide range of Mach number.

For M = 1.5, corresponding to a cross flow Mach number perpendicular to the 40% chord line, M_Ω, of 10/9, a sharp increase in the region of instability occurs even for the cantilever case, $(\omega_\phi/\omega_{\alpha_1})^2 = \infty$. This increase in the region of instability may arise from the use of the linearized supersonic aerodynamic theory at such a low cross flow Mach number. It must be remembered that the Mach number used for the determination of the aerodynamic coefficients of the calculation is the cross flow Mach number, not the free stream Mach number.

The cantilever curves, $(\omega_\phi/\omega_{\alpha_1})^2 = \infty$, of Fig. 1 were determined from two-degree-of-freedom calculations in which first bending and first torsion modes were used without the pitching degree of freedom.

Figure 2 shows curves of the flutter parameters $V_f/\omega_{\alpha_1} b_{0.75}$ and $V_f/\omega_f b_{0.75}$ versus the frequency ratios $(\omega_\phi/\omega_{\alpha_1})$ and (ω_f/ω_{h_1}) calculated by using incompressible aerodynamic coefficients and three degrees of freedom: wing first bending, wing first torsion, and rigid pitch. A sharp increase in the region of instability for values of $(\omega_\phi/\omega_{\alpha_1})$ less than about 0.5 can be seen. More significantly, the decrease in stability appears to be related to the near equality of pitch and bending frequencies. This effect has been observed by other investigators and depends on pitch axis location.

Calculations were also made using an assumed second bending mode along with the first bending, first torsion, and pitch modes and the results are discussed in Appendix I. The addition of the second bending mode does not affect the shape of the flutter boundaries significantly in the Mach number range studied. Changing the ratio of second bending to first torsion frequency, $(\omega_{h_2}/\omega_{\alpha_1})$, from slightly greater than 1.0 to slightly less than 1.0 also has little effect on the flutter boundaries. It appears, then, that sufficient accuracy was obtained

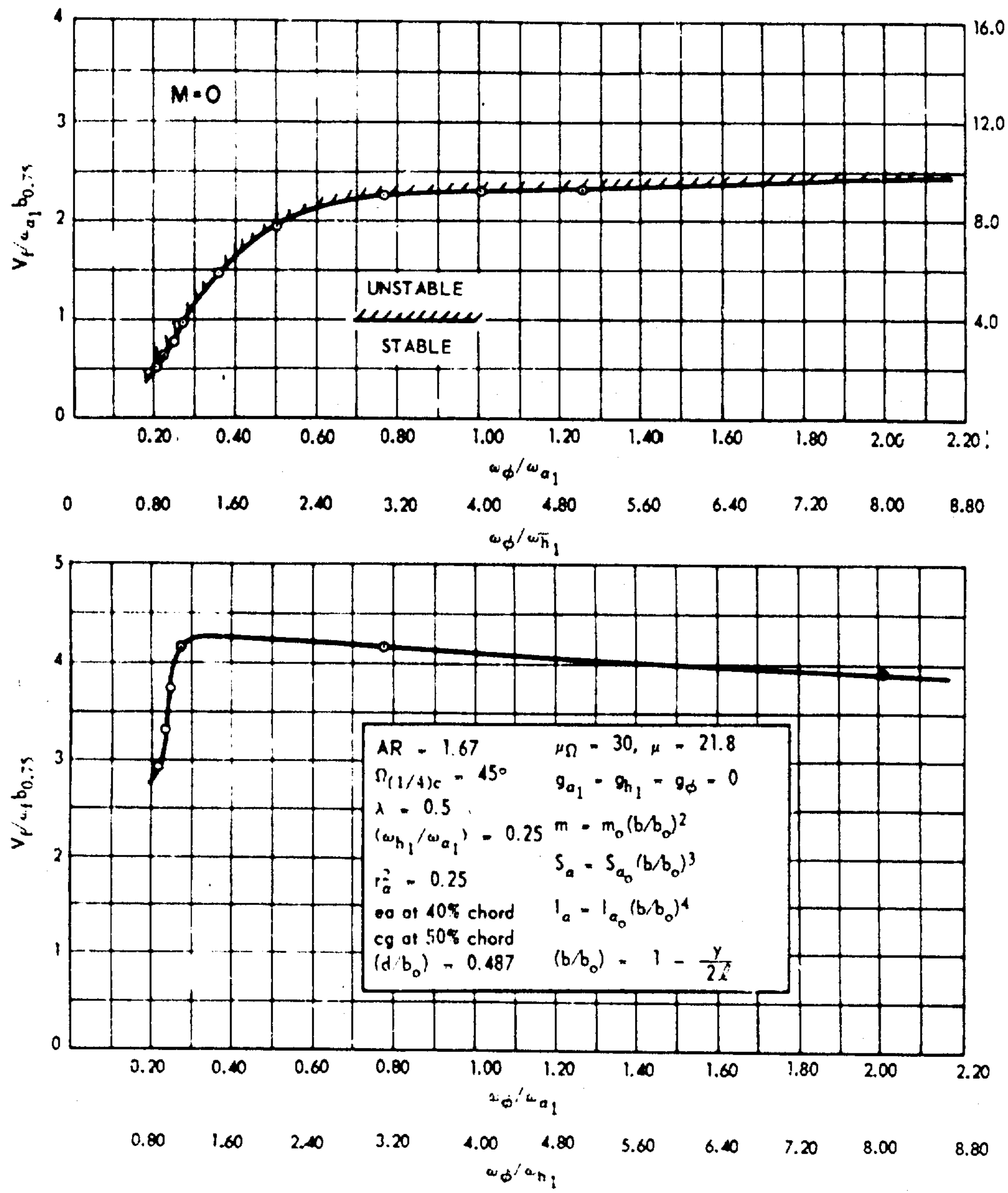

Fig. 2. Flutter parameters $V_f/\omega_{a_1} b_{0.75}$ and $V_f/\omega_f b_{0.75}$ versus $(\omega_\phi/\omega_{a_1})$ and $(\omega_\phi/\omega_{h_1})$ from three-degree-of-freedom incompressible calculation.

in the calculations with three degrees of freedom for the wings studied. As noted in Appendix I, the V-g solutions for the four-degree-of-freedom calculations did furnish valuable insights into the modes of flutter and the effect of structural damping.

2 Discussion of Experimental Results .

During the test program nine cases of flutter occurred for the sixteen configurations tested. Two models fluttered in a cantilever, or "pitch locked," condition and the remaining models at various levels of wing stiffness and pitching frequency.

Reference 1 describes the M. I. T. -WADC supersonic variable Mach number Blow-Down Wind Tunnel facility in which the tests were conducted. Reference 2 describes the techniques of testing that were used to obtain the data. No major changes were necessary in either the wind tunnel facility or the testing techniques to obtain the experimental data presented in this report.

The planform of the stabilizer models tested is shown in Fig. 14 of Appendix II. They incorporated a pitching degree of freedom with a pitch axis perpendicular to the root chord, 64.3% of the root chord aft of the leading edge. The stiffness of the pitching restraint could be varied at will. The model construction was similar to that described in Ref. 2 with a single spar providing the required stiffness. Balsa fairings glued to the spar gave the required 6% thick double wedge airfoil shape and suitably spaced lead weights provided the required mass parameters. A more complete description of the models is given in Appendix II.

Before flutter testing, each model was given vibration and static tests. The results of these tests, as well as the tabulated results of the flutter tests, are contained in Appendix II. With the pitching mechanism "locked out," the cantilever condition, the lowest natural modes of vibration were determined for each model. In general three modes were easily excited, the first bending, first torsion, and second bending modes. The first bending mode and first torsion mode determined in this manner were used to plot the flutter data of Figs. 3 and 4 are the ω_{h_N} and ω_{α_N} of the figures. The rigidities in bending and torsion, EI_r and GJ_r, at the root were also determined for most of the models in the cantilever condition. This data is not too satisfactory since it is difficult to assess accurately the effects of root fitting deformation. As can be seen from Table 2 there seems to be considerable scatter in the EI_r and GJ_r data since models with essentially the same cantilever frequencies appear to have widely different values of EI_r and GJ_r. With the pitching mechanism in operation vibration data was also taken for various pitch restraint stiffnesses. In general, only the first three modes of vibration could be excited easily as can be seen from the data of Table 5. This data furnished the coupled vibration frequencies ω_1 and ω_2 for the plots in Figs. 6 and 7. Influence coefficient data was also taken with the pitching mechanism in operation. The uncoupled pitch frequency, ω_ϕ, was determined from the measured rigidity of the pitch mechanism and from the measured total mass moment of inertia of the wing and root fitting, I_ϕ. A few of the frequencies so determined were checked by fitting a rigid disc of known moment of inertia to the flexure and measuring the resulting vibration frequency. The check on frequencies was satisfactory. Pitching frequency data can be found in Table 3 of Appendix II, while the frequency data and all of the flutter data is summarized in Table 4.

Figures 3, 4, and 5 compare the experimental flutter data and the theoretical predictions when plotted versus Mach number. It is presumed that ω_{α_N}, the first measured cantilever torsion frequency, corresponds fairly closely to the uncoupled first torsion frequency, ω_{α_1}, used as a parameter in the calculations and similarly that ω_{h_N} corresponds closely to ω_{h_1}. Since the different models fluttered at somewhat different relative densities, μ_f, and since the value of μ used in the theory is lower than for most experimental points, the factor $1/\sqrt{\mu_f}$ has been included in the ordinates to reduce the effects of these variations.

The tests of the SWS-2 model, which fluttered in a locked configuration, along with the data of Ref. 3 were used to establish the cantilever, or bending-torsion flutter boundary; $(\omega_\phi/\omega_{h_N})^2$ or $(\omega_\phi/\omega_{\alpha_N})^2 = \infty$. (The SWS-1d model also fluttered in a cantilever condition but, since the vibration data of Table 5 shows that this model had a low torsion frequency quite different from the rest of the stabilizer models, it was used only as a guide in drawing the "locked" boundary.)

The SWS-1 series of models, had a slightly higher stiffness level than SWS-2 and thus had a margin of safety of about 7% in bending-torsion flutter. The margin of safety is defined as the ratio of ω_{α_N} necessary to prevent flutter in the cantilever condition to the ω_{α_N} of the actual model. The SWS-1 series models were flutter-free in the cantilever condition but when the pitch frequency was lowered to about 98 cps, flutter occurred at $M \doteq 1.35$, as can be seen from the SWS-1-98 model test point. Two other SWS-1 series models were flutter tested at lower values of pitch frequency, the SWS-1c-48 and the SWS-1e-74 models. The vibration data shows that these models were similar to the SWS-1-98

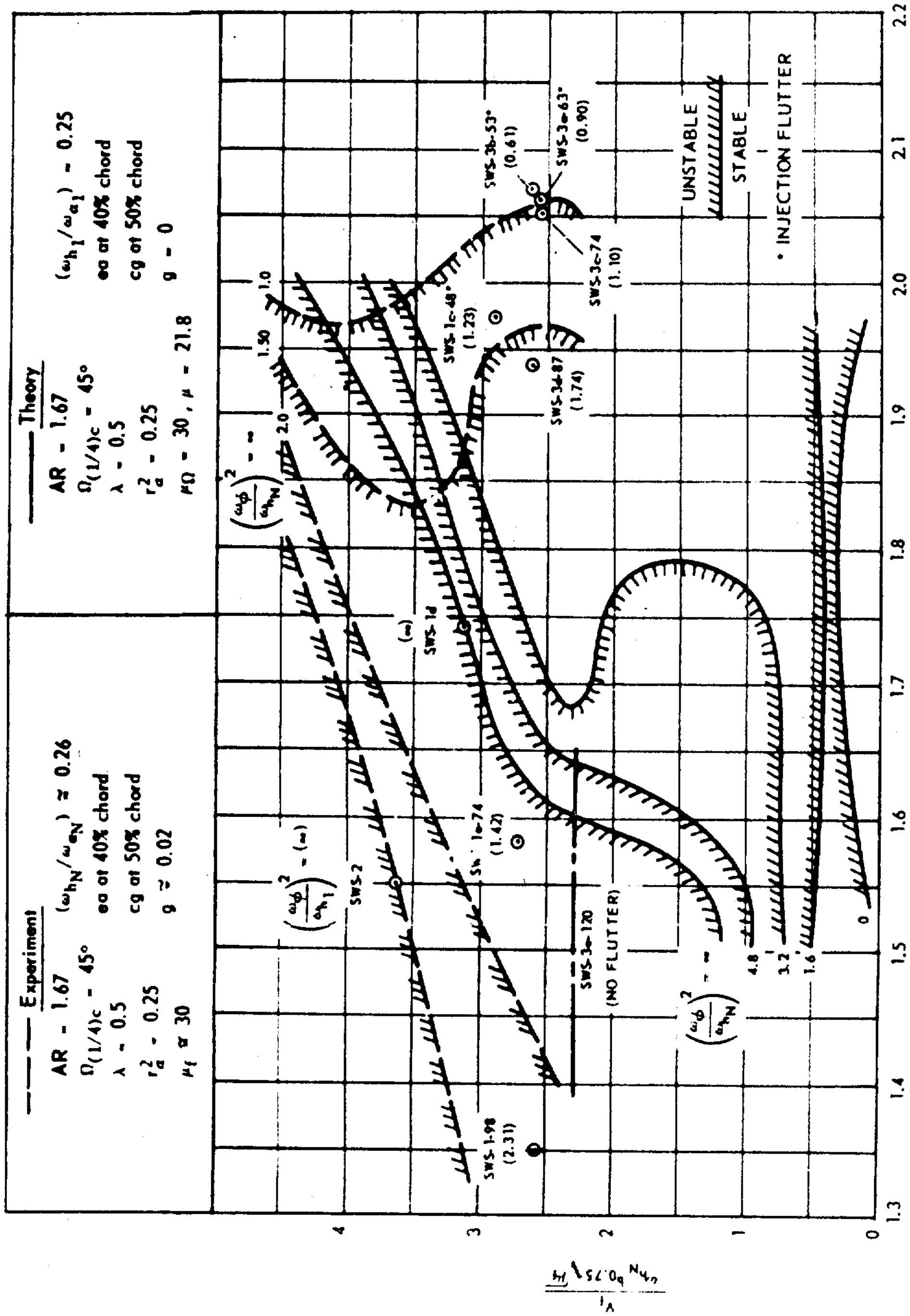

Fig. 3 Flutter parameter $V_f/\omega_{h_N} b_{0.75}\sqrt{\mu_f}$ versus Mach number from experimental tests and comparison with theory.

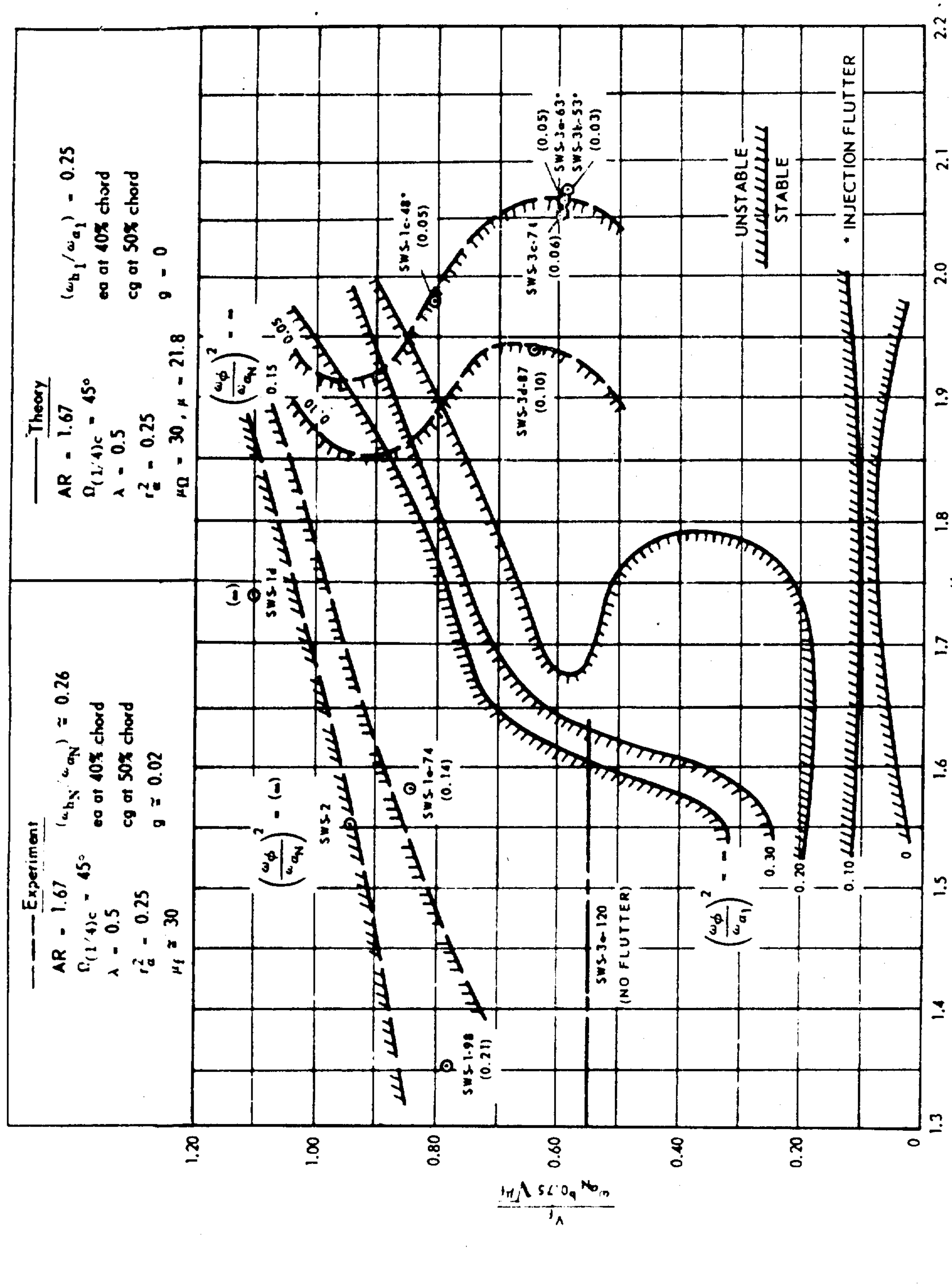

Fig. 4. Flutter parameter $V_f/\omega_{\alpha_N} b_{0.75}\sqrt{\mu_f}$ versus Mach number from experimental tests and comparison with theory.

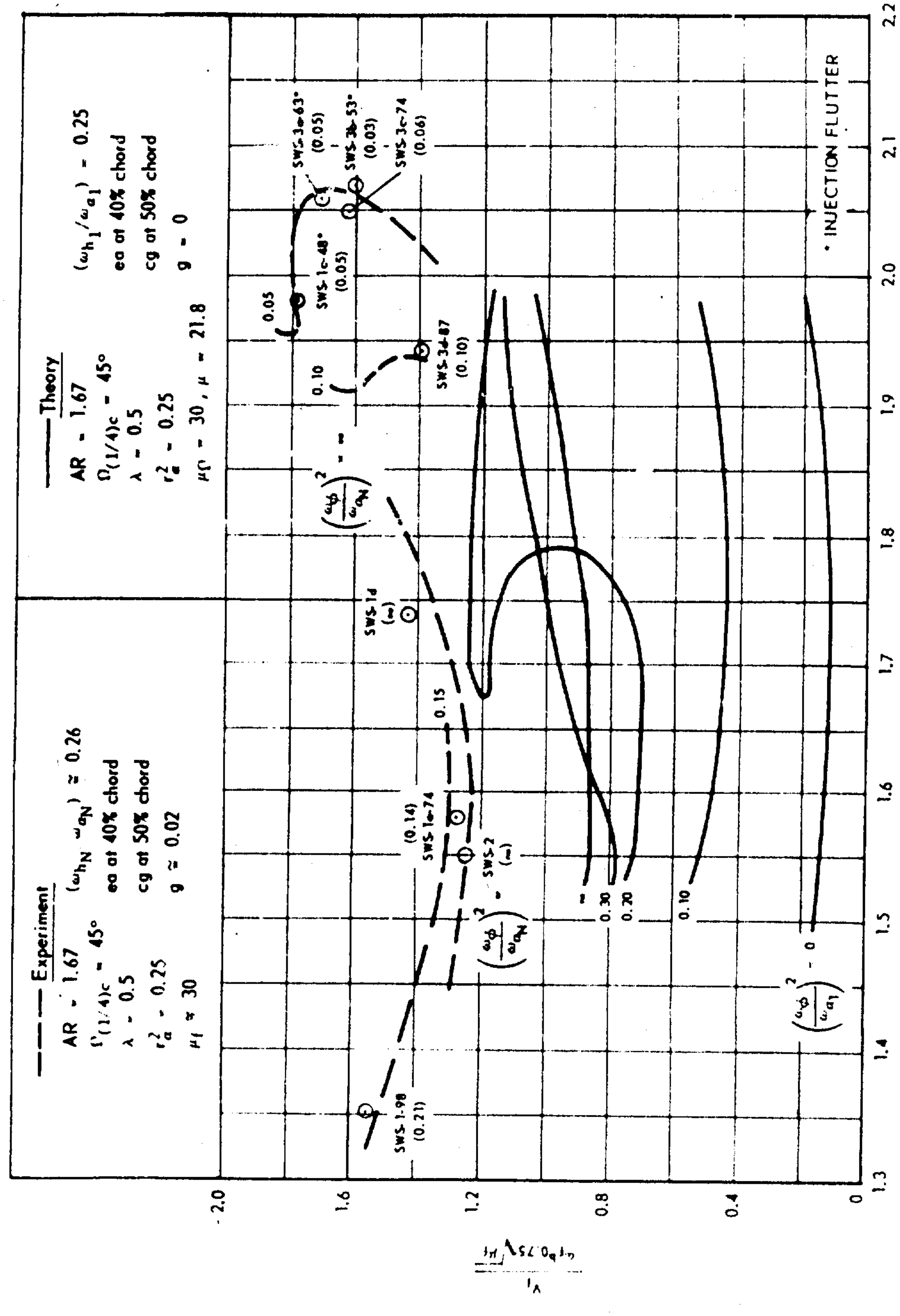

Fig. 5. Flutter parameter $V_f/\omega_f b_{0.75}\sqrt{\mu_f}$ versus Mach number from experimental tests and comparison with theory.

model in a cantilever condition. The SWS-1c-48 model fluttered on injection when practically in the tunnel whereas the SWS-1e-74 model fluttered in the middle of a test run.

The three flutter points for the SWS-1 series models cover quite well the Mach number range available in the wind tunnel so that further tests of this series of models at intermediate values of the pitching frequency were not attempted. Instead a third series of models, SWS-3, were designed with a margin of safety in bending-torsion flutter of about 45% based on the curves of Figs. 3, 4 and 5. In order to achieve the higher frequency and stiffness level required by the increased margin of safety without increasing the model thickness ratio, it was necessary to modify the design parameters of the SWS-3 models. The frequency ratio $(\omega_{h_N} / \omega_{\alpha_N})$ was lowered from an average of 0.29 to 0.26 rather than change the mass parameters. The test data and calculations of Ref. 3 show that there is little variation in the level of the cantilever flutter boundaries for straight and swept wings for variations in $(\omega_{h_N} / \omega_{\alpha_N})$ over this range.

Three of the SWS-3 series models, SWS-3b-53, SWS-3a-63, and SWS-3c-74 fluttered on or very close to injection. The SWS-3c-74 fluttered when fully in the tunnel but before the Mach number had started to change and, therefore, is not shown as an injection flutter. The SWS-3a-63 and the SWS-3b-53 were almost in the tunnel when flutter occurred and are shown as injection flutter. In sketching the experimental boundaries, the data for SWS-3d-87 and SWS-3c-74 were relied on more heavily than the data for SWS-3a-63 and SWS-3b-53.

The SWS-3 series data show that there can be a very large increase in the region of instability if the ratio $(\omega_{\phi} / \omega_{h_N})^2$ is near unity. In fact, it appears that for a given value of $(\omega_{\phi} / \omega_{\alpha_N})^2$ the stiffer SWS-3 models will flutter at higher Mach number than their SWS-1 counter parts. Thus, the experimental boundaries for a given $(\omega_{\phi} / \omega_{h_N})^2$ appear to bend back and form deep "buckets" in the curves just as they do for the calculated results. In general, however, the calculations predict larger regions of instability than the experimental results indicate.

It is interesting to note that the SWS-3 series flutter apparently occur in a different flutter mode than the SWS-1 series. Figures 18 and 19 show the analysis of the high speed movies for the SWS-1-98 and the SWS-3d-87 models, taken from the excerpts from the high speed movies shown in Figs. 16 and 17. The SWS-1-98 model should have a different mode of flutter than the

SWS-3d-87 if the results of Appendix I are correct in that the "buckets" of the boundaries are formed by a new flutter mode. Examination of Figs. 18 and 19 shows that while the relation between the tip vertical translation amplitude to pitch amplitude is of the same order of magnitude for the two models, the relationship between the tip angle of attack amplitude and the pitch amplitude is much different. The SWS-1-98 model shows a much larger ratio of tip angle of attack amplitude to pitch amplitude than does the SWS-3d-87. This fact indicates that the flutter mode for the SWS-1-98 is composed of important pitch-bending-torsion motions while the flutter mode for the SWS-3d-87 is mainly pitch-bending.

It would appear, then, that for small margins of stability in bending-torsion flutter the addition of a high frequency pitch degree of freedom causes a decrease in what is essentially a bending-torsion flutter speed largely because of the decrease in the coupled torsion frequency. However, if (ω_ϕ/ω_h) is low enough to be near unity a bending pitch mode develops which may increase the region of instability to as high as $M = 2$.

Before discussing some of the other curves drawn from the test data, some attention should be given to the SWS-3-53 model. This model, although practically identical with the SWS-3b-53 model insofar as vibration frequencies are concerned, was tested in the same range of Mach number and density as the SWS-3b-53 model but failed to flutter. However, the structural damping of the first two important coupled vibration modes is about twice as great for the SWS-3-53 model (average g of 0.04) as it is for the SWS-3b-53 model (average g of 0.02). The SWS-3 series flutter points form the sharp increases in the regions of instability or "buckets" of Figs. 3, 4 and 5; thus, the mode of flutter may be one that is very sensitive to g variations. Since it was predicted theoretically (Fig. 13) that the mode which forms the "bucket" is very sensitive to changes in g, it then seems possible that the higher structural damping of the SWS-3-53 model may have prevented flutter for this model down to a Mach number of 1.8 where it was destroyed by a failure of the inboard leading edge caused by a root seal failure. This possibility that the "buckets" in the experimental curves are sensitive to g variations may point the way towards elimination of large regions of instability by use of damping. It should be noted that for most of the stabilizer models tested the value of g for the first two important coupled modes is about 0.02.

The data for the SWS-3e-120 model is also particularly interesting because this model failed to flutter over the Mach number range 1.25 to 2.00. This failure to flutter means that the curve for $(\omega_\phi/\omega_{h_N})^2 = 0.16$ must be drawn as shown in Figs. 3, 4 and 5 and shows that at these higher values of $(\omega_\phi/\omega_{h_N})$ the "bucket" is not evident. Comparison of the data for the SWS-3e-120 and the other SWS-3 models helps to set upper and lower limits of $(\omega_\phi / \omega_{\alpha_N})$ for flutter in the Mach number range 1.27 to 2.10.

In Fig. 6 and Fig. 7 the first two coupled frequencies with the pitching mechanism in operation, ω_1 and ω_2, were used to form the flutter parameters $(b_{0.75}\omega_1/a_f)\sqrt{(\mu/65)_{0.75}}$ and $(b_{0.75}\omega_2/a_f)\sqrt{(\mu/65)_{0.75}}$, where a_f is the speed of sound at flutter. The use of the relative density correction in this form is based on the previous experimental results of Ref. 3 and not on any firm theoretical basis. Figures 6 and 7 may be useful as design charts; a straight line parallel to the abscissa being a constant altitude line, and a straight line from the suppressed origin being a line of constant dynamic pressure.

In Fig. 6, the first coupled vibration frequency, ω_1, is used to normalize the data. This vibration mode, as can be seen from Table 5, is essentially a combination of the rigid pitch and the first bending modes of the model. The SWS-1e-74 and the SWS-3d-87 both have the same value of the parameter (ω_ϕ/ω_1) and hence must fall along the same boundary. Thus, the curves must be drawn as shown in Fig. 6 with a narrow stable region between the $(\omega_\phi/\omega_1) = \infty$ and the $(\omega_\phi/\omega_1) = 1.60$ curve.

Figure 7 shows curves similar to those of Fig. 6 except that the second coupled vibration frequency, ω_2, is used as a parameter. This vibration mode, as can be seen from the data of Table 5 is largely a combination of the rigid pitch and first torsion modes of the model except for the lowest pitch restraint stiffnesses where it may involve appreciable bending.

For the various experimental plots, curves have been drawn on the basis of a bare minimum of data. The fairing of such curves is subject to some question, and Figs. 3, 4, 5, 6, and 7 therefore represent only rough sketches of where the flutter boundaries lie. The general outlines of the curves are probably correct, and enough experimental data has been obtained to show that there are large increases in the regions of instability with sufficiently low values of the pitching frequency. Furthermore, these increases appear to follow the general trends established by the theoretical results.

In one respect the theoretical results do not match the experimental results even qualitatively. This is at the lower Mach number of the calculation $M = 1.52$ or $M_\Omega = 10/9$. For this case the calculated results show that even the "locked" case has a sharp increase in the region of instability and predicts that the SWS-1 and the SWS-3 series models will flutter in the cantilever or "locked" configuration. The failure of the theoretical calculations to predict flutter correctly in this regime is probably due to the failure of the linearized aerodynamic theory to predict aerodynamic forces correctly in the high-transonic - low supersonic

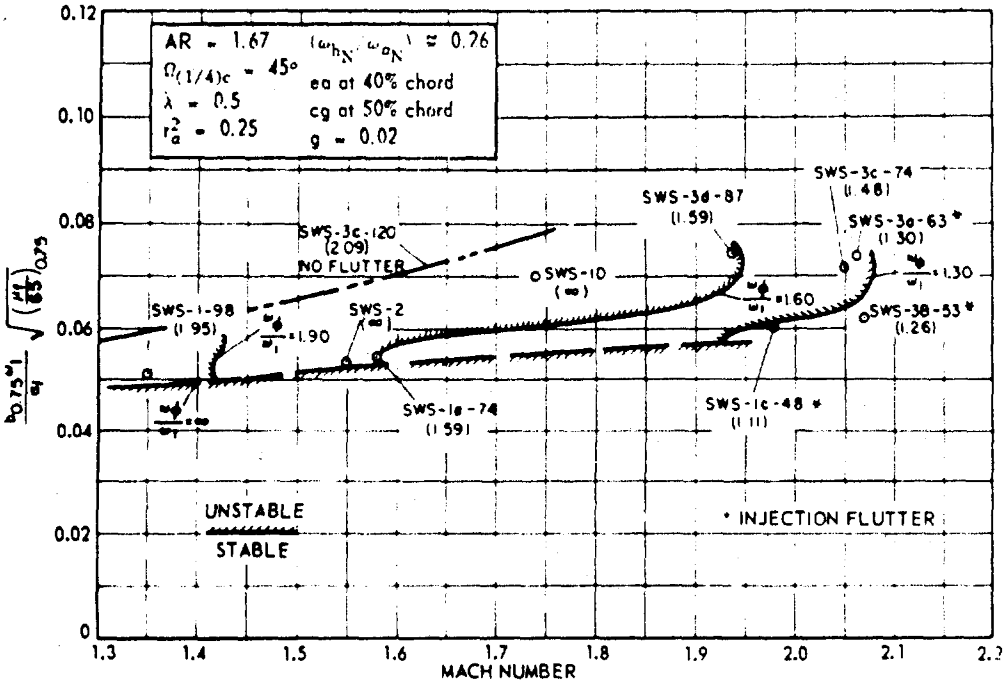

Fig. 6. Flutter parameter $(b_{0.75}\omega_2/a_f)\sqrt{(\mu_f/65)_{0.75}}$ versus Mach number from experimental tests.

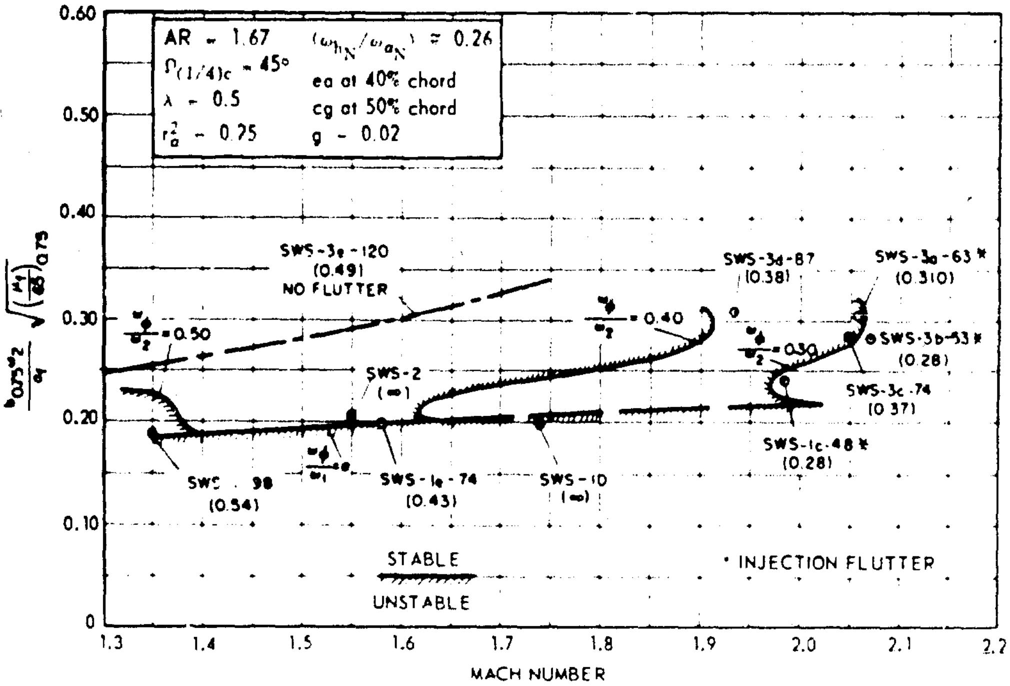

Fig. 7. Flutter parameter $(b_{0.75}\omega_2/a_f)\sqrt{(\mu_f/65)_{0.75}}$ versus Mach number from experimental tests.

regime. Similarly, it seems probable that the failure of the theoretical calculations to make good quantitative predictions throughout the Mach number range for the various pitching frequencies and model stiffnesses is due to the failure of the aerodynamic terms in describing accurately the actual forces on the wing.

SECTION III

CONCLUSIONS

Some conclusions may be drawn from the theoretical and the experimental results of the present program. They may be summarized as follows:

1. Three basic assumed modes appear to be sufficient to define qualitatively the flutter boundaries when the velocity-component method of Ref. 8 is used. These modes are wing first bending, wing first torsion, and rigid pitch. Addition of wing second bending does not change the results of the calculation significantly.
2. For low margins of safety in bending-torsion flutter, the inclusion of a high frequency pitch mode results in minor reductions in flutter speed.
3. For both low (7%) and high (45%) margins of safety in bending-torsion flutter, the inclusion of a critical pitch mode ($\omega_\phi/\omega_h \cong 1$) causes large regions of instability in an essentially pitch-bending flutter mode which may extend as high as M = 2.
4. The theoretical calculations do not give a good quantitative correlation with the experimental results. The theoretical calculations predict larger regions of instability than are observed experimentally. They also predict that the rapid increases in the regions of instability will occur at higher values of (ω_ϕ/ω_{h_1}) than were observed experimentally.
5. The theoretical calculations indicate that the mode of flutter which causes the large increases in the region of instability may be very sensitive to changes in structural damping coefficient. Some of the test data obtained from the SWS-3 series models confirm this conclusion.

BIBLIOGRAPHY

1. Halfman, R. L., McCarthy, J. F., Jr., Prigge, J. S.,Jr., Wood, G. A.,Jr., A Variable Mach Number Supersonic Test Section for Flutter Research, WADC Technical Report 54-114, December, 1954.

2. McCarthy, J. F., Jr., Asher, G. W., Prigge, J. S., Jr., Levey, G. M., Three-Dimensional Supersonic Flutter Model Tests Near Mach Number 1.5, Part I, Model Design and Testing Techniques, WADC Technical Report 54-113, Part I, December, 1955.

3. McCarthy, J. F., Jr., Zartarian, G., Martuccelli, J. R., Asher, G.W., Three-Dimensional Supersonic Flutter Model Tests Near Mach Number 1.5, Part II, Experimental and Theoretical Data for Bare Wings and Wings with Tip Tanks, WADC Technical Report 54-113, Part II, to be published (Confidential).

4. Jones, G. W., Jr., DuBose, H. C., Investigation of Wing Flutter at Transonic Speeds for Six Systematically Varied Wing Plan Forms, NACA RM L53G10a, August 13, 1953 (Confidential).

5. Zartarian, G., Hsu, P. T., Theoretical Studies on the Prediction of Unsteady Supersonic Airloads on Elastic Wings, Part I, Investigations on the Use of Oscillatory Supersonic Aerodynamic Influence Coefficients, WADC Technical Report 56-97, Part I, December 1955 (Confidential, Title Unclassified).

6. Zartarian, G., Theoretical Studies on the Prediction of Unsteady Supersonic Airloads on Elastic Wings, Part II, Rules for Application of Oscillating Supersonic Aerodynamic Influence Coefficients, WADC Technical Report 56-97, Part II, February 1956 (Confidential, Title Unclassified).

7. Spielberg, I., Fettis, H. E., Toney, H. S., Methods for Calculating the Flutter and Vibration Characteristics of Swept Wings, M. R. No. MCREXA5-4595-8-4, Air Materiel Command, USAF, August 3, 1948.

8. Barmby, J. G., Cunningham, H. J., Garrick, I. E., Study of the Effects of Sweep on the Flutter of Cantilever Wings, NACA Technical Report 1014, 1951.

9. Scanlon, R. T., Rosenbaum, R., Aircraft Vibration and Flutter, First Edition, The MacMillan Co., New York, 1951.

10. Smilg, B., Wasserman, L. S., Application of Three-Dimensional Flutter Theory to Aircraft Structures, U. S. Army Air Corps, Technical Report 4798, July, 1942.

APPENDIX I

THEORETICAL CALCULATIONS

1 Introduction

In setting up the flutter equations for the all-movable swept stabilizer, the authors examined the relative merits of the strip-theory method (Ref. 7) and the velocity-component method (Ref. 8). For the strip-theory method, the aerodynamic forces are applied to sections parallel to the free-stream while for the velocity-component method, they are applied to sections normal to the elastic axis. The former method is more rational when the wing ribs are parallel to the free stream, and gives a better representation of the aerodynamic conditions at the root and wing tip. The latter method, however, appears to be more suitable for the swept stabilizer model which derives all its stiffness characteristics from a single spar. The simple spar type of construction, the relatively high length to chord ratio as well as the results of vibration tests suggest that the concept of the root being effectively clamped perpendicular to the elastic axis, which is a basic assumption of the velocity-component method, is well justified. Therefore, it was decided that the velocity-component method would be used in deriving the equations of motion.

In the derivation and solution of the equations of motion by the velocity component method all quantities, mass parameters and aerodynamic forces, are referred to a reference system (x_{Ω}, y_{Ω}) swept with the elastic axis (Fig. 8). In particular the Mach number used in obtaining the aerodynamic coefficients must be the crossflow Mach number M_{Ω}. In the presentation of the results, however, all the theoretical flutter parameters have been referred to an unswept reference system (x, y) for convenience when comparing with experimental results.

2. Flutter Equations Based on Velocity-Component Method

The flutter equations are derived following the method of Section 16.2 of Ref. 9. The assumption that the wing displacement is a superposition of four modes gives as the deflection of any point (Fig. 8)

$$Z_a(x_\Omega, y_\Omega, t) = F_{h_1}(y_\Omega)\bar{h}_1(t) + F_{h_2}(y_\Omega)\bar{h}_2(t) + x_\Omega F_\alpha(y_\Omega)\bar{\alpha}_\Omega(t)$$

$$+ (y_\Omega \sin\Omega + x_\Omega \cos\Omega - d)\,\bar{\phi}\,(t) \tag{1}$$

where (see Eqs. 40-42)

F_{h_1}, F_{h_2} are the first and second assumed cantilever bending modes

F_α is the first assumed uncoupled torsion mode

$\left.\begin{matrix}\bar{h}_1,\ \bar{h}_2 \\ \bar{\alpha}_\Omega,\ \bar{\phi}\end{matrix}\right\}$ are reference tip amplitudes for the first and second bending modes, first uncoupled torsion mode, and rigid body pitch mode, respectively.

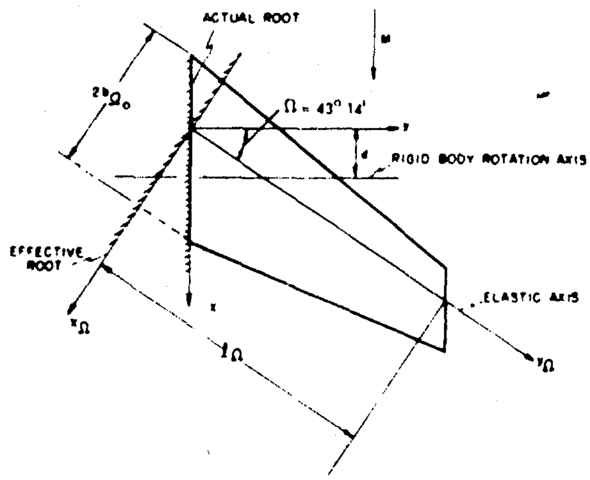

Fig. 8. Axis system for swept stabilizer.

From Eq. (1) it is seen that the rigid body pitch is equivalent to a bending of the elastic axis plus a rotation about the elastic axis, so that only the aerodynamic forces due to the translation and rotation of sections normal to the elastic axis are needed. Application of the Lagrange equations of motion to the system as given by Fig. 8 along with the assumption of simple harmonic motion and the introduction of the dimensionless variable

$$\eta_\Omega = \frac{y_\Omega}{l_\Omega} \tag{2}$$

leads to the following dimensionless set of flutter equations:

$$A\left(\frac{\bar{h}_1}{b_{\Omega_0}}\right) + B\left(\frac{\bar{h}_2}{b_{\Omega_0}}\right) + C\bar{\alpha} + D\bar{\phi} = 0 \tag{3}$$

$$E\left(\frac{\bar{h}_1}{b_{\Omega_0}}\right) + F\left(\frac{\bar{h}_2}{b_{\Omega_0}}\right) + G\bar{\alpha}_\Omega + H\bar{\phi} = 0 \tag{4}$$

$$I\left(\frac{\bar{h}_1}{b_{\Omega_0}}\right) + J\left(\frac{\bar{h}_2}{b_{\Omega_0}}\right) + K\bar{\alpha}_\Omega + L\bar{\phi} = 0 \tag{5}$$

$$M\left(\frac{\bar{h}_1}{b_{\Omega_0}}\right) + N\left(\frac{\bar{h}_2}{b_{\Omega_0}}\right) + O\bar{\alpha}_\Omega + P\bar{\phi} = 0 \tag{6}$$

where

$$A = \left\{ \int_0^1 \left(\frac{b_\Omega}{b_{\Omega_0}}\right)^2 L_{hh} F_{h_1}^2 \, d\eta_\Omega + \int_0^1 \left(\frac{b_\Omega}{b_{\Omega_0}}\right)^3 \left(\frac{b_{\Omega_0}}{\ell_\Omega}\right) \frac{dF_{h_1}}{d\eta_\Omega} L_{hh'} F_{h_1} \, d\eta_\Omega + \left[1 - \left(\frac{\omega_{h_1}}{\omega_{\alpha_1}}\right)^2 Z\right] \int_0^1 \left(\frac{b_\Omega}{b_{\Omega_0}}\right)^2 \mu_\Omega F_{h_1}^2 \, d\eta_\Omega \right\} \tag{7}$$

$$B = \left\{ \int_0^1 \left(\frac{b_\Omega}{b_{\Omega_0}}\right)^2 L_{hh} F_{h_1} F_{h_2} \, d\eta_\Omega + \int_0^1 \left(\frac{b_\Omega}{b_{\Omega_0}}\right)^3 \left(\frac{b_{\Omega_0}}{\ell_\Omega}\right) \frac{dF_{h_2}}{d\eta_\Omega} L_{hh'} F_{h_1} \, d\eta_\Omega + \int_0^1 \left(\frac{b_\Omega}{b_{\Omega_0}}\right)^2 \mu_\Omega F_{h_1} F_{h_2} \, d\eta_\Omega \right\} \tag{8}$$

$$C = \left\{ \int_0^1 \left(\frac{b_\Omega}{b_{\Omega_0}}\right)^3 L_{h\alpha} F_\alpha F_{h_1} \, d\eta_\Omega + \int_0^1 \left(\frac{b_\Omega}{b_{\Omega_0}}\right)^4 \left(\frac{b_{\Omega_0}}{\ell_\Omega}\right) \frac{dF_\alpha}{d\eta_\Omega} L_{h\alpha'} F_{h_1} \, d\eta_\Omega + \int_0^1 \left(\frac{b_\Omega}{b_{\Omega_0}}\right)^3 \mu_\Omega x_{\alpha_\Omega} F_{\alpha_\Omega} F_{h_1} \, d\eta_\Omega \right\} \tag{9}$$

$$D = \left\{ \int_0^1 \left(\frac{b_\Omega}{b_{\Omega_0}}\right)^3 L_{h\phi}\, F_{h_1}\, d\eta_\Omega + \cos \int_0^1 \left(\frac{b_\Omega}{b_{\Omega_0}}\right)^3 \mu_\Omega x_{\alpha_\Omega} F_{h_1}\, d\eta_\Omega \right.$$

$$\left. - \int_0^1 \left(\frac{d}{b_{\Omega_0}}\right)\left(\frac{b_\Omega}{b_{\Omega_0}}\right)^2 \mu_\Omega F_{h_1}\, d\eta_\Omega \right\} \quad (10)$$

$$E = \left\{ \int_0^1 \left(\frac{b_\Omega}{b_{\Omega_0}}\right) L_{hh} F_{h_1} F_{h_2}\, d\eta_\Omega + \int_0^1 \left(\frac{b_\Omega}{b_{\Omega_0}}\right)^3 \left(\frac{b_{\Omega_0}}{\ell_\Omega}\right) \frac{dF_{h_1}}{d\eta_\Omega} L_{hh'} F_{h_2}\, d\eta_\Omega \right.$$

$$\left. + \int_0^1 \left(\frac{b_\Omega}{b_{\Omega_0}}\right)^2 \mu_\Omega F_{h_1} F_{h_2}\, d\eta_\Omega \right\} \quad (11)$$

$$F = \left\{ \int_0^1 \left(\frac{b_\Omega}{b_{\Omega_0}}\right)^2 L_{hh} F_{h_2}^2\, d\eta_\Omega + \int_0^1 \left(\frac{b_\Omega}{b_{\Omega_0}}\right)^3 \left(\frac{b_{\Omega_0}}{\ell_\Omega}\right) \frac{dF_{h_2}}{d\eta_\Omega} L_{hh'} F_{h_2}\, d\eta_\Omega \right.$$

$$\left. + \left[1 - \left(\frac{\omega_{h_2}}{\omega_{\alpha 1}}\right)^2 Z\right] \int_0^1 \left(\frac{b_\Omega}{b_{\Omega_0}}\right)^2 \mu_\Omega F_{h_2}^2\, d\eta_\Omega \right\} \quad (12)$$

$$G = \left\{ \int_0^1 \left(\frac{b_\Omega}{b_{\Omega_0}}\right)^3 L_{h\alpha} F_\alpha F_{h_2}\, d\eta_\Omega + \int_0^1 \left(\frac{b_\Omega}{b_{\Omega_0}}\right)^4 \left(\frac{b_{\Omega_0}}{\ell_\Omega}\right) \frac{dF_\alpha}{d\eta_\Omega} L_{h\alpha'} F_{h_2}\, d\eta_\Omega \right.$$

$$\left. + \int_0^1 \left(\frac{b_\Omega}{b_{\Omega_0}}\right)^3 \mu_\Omega x_{\alpha_\Omega} F_\alpha F_{h_2}\, d\eta_\Omega \right\} \quad (13)$$

$$H = \left\{ \int_0^1 \left(\frac{b_\Omega}{b_{\Omega_0}}\right)^3 L_{h\phi} F_{h_2}\, d\eta_\Omega + \cos\Omega \int_0^1 \left(\frac{b_\Omega}{b_{\Omega_0}}\right)^3 \mu_\Omega x_{\alpha_\Omega} F_{h_2}\, d\eta_\Omega \right.$$

$$\left. - \int_0^1 \left(\frac{d}{b_{\Omega_0}}\right)\left(\frac{b_\Omega}{b_{\Omega_0}}\right)^2 \mu_\Omega F_{h_2}\, d\eta_\Omega \right\} \quad (14)$$

$$I = \left\{ \int_0^1 \left(\frac{b_\Omega}{b_{\Omega_0}}\right)^3 M_{\alpha h} F_\alpha F_{h_1} \, d\eta_\Omega + \int_0^1 \left(\frac{b_\Omega}{b_{\Omega_0}}\right)^4 \left(\frac{b_{\Omega_0}}{\ell_\Omega}\right) \frac{dF_{h_1}}{d\eta_\Omega} M_{\alpha h'} F_\alpha d\eta_\Omega \right.$$

$$\left. + \int_0^1 \left(\frac{b_\Omega}{b_{\Omega_0}}\right)^3 \mu_\Omega \, x_{\alpha_\Omega} F_\alpha F_{h_1} \, d\eta_\Omega \right\} \quad (15)$$

$$J = \left\{ \int_0^1 \left(\frac{b_\Omega}{b_{\Omega_0}}\right)^3 M_{\alpha h} F_\alpha F_{h_2} d\eta_\Omega + \int_0^1 \left(\frac{b_\Omega}{b_{\Omega_0}}\right)^4 \left(\frac{b_{\Omega_0}}{\ell_\Omega}\right) \frac{dF_{h_2}}{d\eta_\Omega} M_{\alpha h'} F_\alpha d\eta_\Omega \right.$$

$$\left. + \int_0^1 \left(\frac{b_\Omega}{b_{\Omega_0}}\right)^3 \mu_\Omega \, x_{\alpha_\Omega} F_\alpha F_{h_2} d\eta_\Omega \right\} \quad (16)$$

$$K = \left\{ \int_0^1 \left(\frac{b_\Omega}{b_{\Omega_0}}\right)^4 M_{\alpha\alpha} F_\alpha^2 \, d\eta_\Omega + \int_0^1 \left(\frac{b_\Omega}{b_{\Omega_0}}\right)^5 \left(\frac{b_{\Omega_0}}{\ell_\Omega}\right) \frac{dF_\alpha}{d\eta_\Omega} M_{\alpha\alpha'} F_\alpha d\eta_\Omega \right.$$

$$\left. + [1 - Z] \int_0^1 \left(\frac{b_\Omega}{b_{\Omega_0}}\right)^4 \mu_\Omega r_{\alpha_\Omega}^2 F_\alpha^2 \, d\eta_\Omega \right\} \quad (17)$$

$$L = \left\{ \int_0^1 \left(\frac{b_\Omega}{b_{\Omega_0}}\right)^4 M_{\alpha\phi} F_\alpha d\eta_\Omega - \int_0^1 \left(\frac{d_\Omega}{b_{\Omega_0}}\right) \left(\frac{b_\Omega}{b_{\Omega_0}}\right)^3 \mu_\Omega x_{\alpha_\Omega} F_\alpha d\eta_\Omega \right.$$

$$\left. + \cos\Omega \int_0^1 \left(\frac{b_\Omega}{b_{\Omega_0}}\right)^4 \mu_\Omega \, r_{\alpha_\Omega}^2 F_\alpha d\eta_\Omega \right\} \quad (18)$$

$$M = \left\{ \cos\Omega \int_0^1 \left(\frac{b_\Omega}{b_{\Omega_0}}\right)^3 M_{\alpha h} F_{h_1}\, d\eta_\Omega + \cos\Omega \int_0^1 \left(\frac{b_\Omega}{b_{\Omega_0}}\right)^4 \left(\frac{b_{\Omega_0}}{\ell_\Omega}\right) \frac{dF_{h_1}}{d\eta_\Omega} M_{\alpha h'} d\eta_\Omega \right.$$

$$- \int_0^1 \left(\frac{d}{b_{\Omega_0}}\right) \left(\frac{b_\Omega}{b_{\Omega_0}}\right)^2 L_{hh} F_{h_1} d\eta_\Omega - \int_0^1 \left(\frac{d}{b_{\Omega_0}}\right) \left(\frac{b_\Omega}{b_{\Omega_0}}\right)^3 \left(\frac{b_{\Omega_0}}{\ell_\Omega}\right) \frac{dF_{h_1}}{d\eta_\Omega} L_{hh'} d\eta_\Omega$$

$$\left. - \int_0^1 \left(\frac{d}{b_{\Omega_0}}\right) \left(\frac{b_\Omega}{b_{\Omega_0}}\right)^2 \mu_\Omega F_{h_1} d\eta_\Omega + \cos\Omega \int_0^1 \left(\frac{b_\Omega}{b_{\Omega_0}}\right)^3 \mu_\Omega x_{\alpha_\Omega} F_{h_1} d\eta_\Omega \right\} \tag{19}$$

$$N = \left\{ \cos\Omega \int_0^1 \left(\frac{b_\Omega}{b_{\Omega_0}}\right)^3 M_{\alpha h} F_{h_2} d\eta_\Omega + \cos\Omega \int_0^1 \left(\frac{b_\Omega}{b_{\Omega_0}}\right)^4 \left(\frac{b_{\Omega_0}}{\ell_\Omega}\right) \frac{dF_{h_2}}{d\eta_\Omega} M_{\alpha h'} d\eta_\Omega \right.$$

$$- \int_0^1 \left(\frac{d}{b_{\Omega_0}}\right) \left(\frac{b_\Omega}{b_{\Omega_0}}\right)^2 L_{hh} F_{h_2} d\eta_\Omega - \int_0^1 \left(\frac{d}{b_{\Omega_0}}\right) \left(\frac{b_\Omega}{b_{\Omega_0}}\right)^3 \left(\frac{b_{\Omega_0}}{\ell_\Omega}\right) \frac{dF_{h_2}}{d\eta_\Omega} L_{hh'} d\eta_\Omega$$

$$\left. - \int_0^1 \left(\frac{d}{b_{\Omega_0}}\right) \left(\frac{b_\Omega}{b_{\Omega_0}}\right)^2 \mu_\Omega F_{h_2} d\eta_\Omega + \cos\Omega \int_0^1 \left(\frac{b_\Omega}{b_{\Omega_0}}\right)^3 \mu_\Omega x_{\alpha_\Omega} F_{h_2} d\eta_\Omega \right\} \tag{20}$$

$$O = \left\{ \cos\Omega \int_0^1 \left(\frac{b_\Omega}{b_{\Omega_0}}\right)^4 M_{\alpha\alpha} F_\alpha d\eta_\Omega + \cos\Omega \int_0^1 \left(\frac{b_\Omega}{b_{\Omega_0}}\right)^5 \left(\frac{b_{\Omega_0}}{\ell_\Omega}\right) \frac{dF_\alpha}{d\eta_\Omega} M_{\alpha\alpha'} d\eta_\Omega \right.$$

$$- \int_0^1 \left(\frac{d}{b_{\Omega_0}}\right) \left(\frac{b_\Omega}{b_{\Omega_0}}\right)^3 L_{h\alpha} F_\alpha d\eta_\Omega - \int_0^1 \left(\frac{d}{b_{\Omega_0}}\right) \left(\frac{b_\Omega}{b_{\Omega_0}}\right)^4 \left(\frac{b_{\Omega_0}}{\ell_\Omega}\right) \frac{dF_\alpha}{d\eta_\Omega} L_{h\alpha'} d\eta_\Omega$$

$$\left. - \int_0^1 \left(\frac{d}{b_{\Omega_0}}\right) \left(\frac{b_\Omega}{b_{\Omega_0}}\right)^3 \mu_\Omega x_{\alpha_\Omega} F_\alpha d\eta_\Omega + \cos\Omega \int_0^1 \left(\frac{b_\Omega}{b_{\Omega_0}}\right)^4 \mu_\Omega r^2_{\alpha_\Omega} F_\alpha d\eta_\Omega \right\} \tag{21}$$

$$P = \left\{ \cos\Omega \int_0^1 \left(\frac{b_\Omega}{b_{\Omega_0}}\right)^4 M_{\alpha\phi}\, d\eta_\Omega - \int_0^1 \left(\frac{d}{b_{\Omega_0}}\right)\left(\frac{b_\Omega}{b_{\Omega_0}}\right)^3 L_{h\phi}\, d\eta_\Omega \right.$$

$$\left[1 - \left(\frac{\omega_\phi}{\omega_{\alpha_1}}\right)^2 Z\right]\left[\int_0^1 \left(\frac{d}{b_{\Omega_0}}\right)^2 \left(\frac{b_\Omega}{b_{\Omega_0}}\right)^2 \mu_\Omega\, d\eta_\Omega + \cos^2\Omega \int_0^1 \left(\frac{b_\Omega}{b_{\Omega_0}}\right)^4 \mu_\Omega r^2_{\alpha_\Omega}\, d\eta_\Omega \right.$$

$$\left. \left. - 2\cos\Omega \int_0^1 \left(\frac{d}{b_{\Omega_0}}\right)\left(\frac{b_\Omega}{b_{\Omega_0}}\right)^3 \mu_\Omega x_{\alpha_\Omega}\, d\eta_\Omega \right] \right\} \tag{22}$$

and

$$Z = \left(\frac{\omega_{\alpha_1}}{\omega_f}\right)^2 \tag{23}$$

$$\mu_\Omega = \frac{m_\Omega}{\pi\rho b^2_\Omega} \quad \text{(constant along span)} \tag{24}$$

$$x_{\alpha_\Omega} = \frac{S_{\alpha_\Omega}}{m_\Omega b_\Omega} \quad \text{(constant along span)}$$

$$r^2_{\alpha_\Omega} = \frac{I_{\alpha\Omega}}{m_\Omega b^2_\Omega} \quad \text{(constant along span)} \tag{25}$$

The aerodynamic coefficients are, as defined in Ref. 9:

$$L_{hh} = L_h \tag{26}$$

$$L_{hh'} = -i\,\frac{\tan\Omega}{k} L_h \tag{27}$$

$$L_{h\alpha} = L_\alpha - L_h\left(\frac{1}{2} + a\right) \tag{28}$$

$$L_{h\alpha'} = -i\,\frac{\tan\Omega}{k}\left[-\frac{1}{2} + L_h\left(\frac{1}{2} - a\right)\right] \tag{29}$$

$$M_{\alpha h} = M_h - L_h\left(\frac{1}{2} + a\right) \tag{30}$$

$$M_{\alpha h'} = -i\,\frac{\tan\Omega}{k}\left[M_h - L_h\left(\frac{1}{2} + a\right)\right] \tag{31}$$

$$M_{\alpha\alpha} = M_\alpha - (M_h + L_\alpha)(\frac{1}{2} + a) + L_h(\frac{1}{2} + a)^2 \qquad (32)$$

$$M_{\alpha\alpha'} = -i\,\frac{\tan\Omega}{k}\,[\,\frac{3}{8} - i\,\frac{1}{2k} - L_h(\frac{1}{4} - a^2)\,]^* \qquad (33)$$

$$L_{h\phi} = \left[\frac{y_\Omega \sin\Omega - d}{b_\Omega}\right] L_{hh} + L_{h\alpha}\cos\Omega + L_{hh'}\sin\Omega \qquad (34)$$

$$M_{\alpha\phi} = \left[\frac{y_\Omega \sin\Omega - d}{b_\Omega}\right] M_{\alpha h} + M_{\alpha\alpha}\cos\Omega + M_{\alpha h'}\sin\Omega \qquad (35)$$

where L_h, L_α, M_α and M_h are as defined by Ref. 10.

The above equations were written using the actual mass distribution for the stabilizer being studied. These relationships are

$$m_\Omega = m_{\Omega_0}\left(\frac{b_\Omega}{b_{\Omega_0}}\right)^2 \qquad (36)$$

$$S_{\alpha_\Omega} = x_{\alpha_\Omega} m_{\Omega_0}\,\frac{{b_\Omega}^3}{{b_{\Omega_0}}^2} \qquad (37)$$

$$I_{\alpha_\Omega} = r^2_{\alpha_\Omega}\, m_{\Omega_0}\,\frac{b^4_\Omega}{b^2_{\Omega_0}} \qquad (38)$$

where

$$\left(\frac{b_\Omega}{b_{\Omega_0}}\right) = \left(1 - \frac{y_\Omega}{2\ell_\Omega}\right) \qquad (39)$$

However, to simplify the aerodynamic calculations, the tapered planform was replaced by a rectangular planform of constant chord so that the aerodynamic coefficients would remain constant along the span at a given value of reduced frequency. A check calculation has shown that if reference semichord, b_r, is taken at the 75% span station of the actual mode perpendicular to the elastic axis, the difference between the values of the aerodynamic integrals as given by the rectangular

---

*It should be noted that this equation is given incorrectly in Ref. 9.

planform and those values found by an actual numerical integration along the span of the tapered wing are very small.

The first bending mode was taken as

$$F_{h_1} = \eta_{\Omega}^2 \tag{40}$$

the first torsion as

$$F_{\alpha} = \eta_{\Omega} \tag{41}$$

and second bending as

$$F_{h_2} = -12.209\,\eta_{\Omega}^2 + 25.488\,\eta_{\Omega}^3 - 12.279\,\eta_{\Omega}^4 \tag{42}$$

The second bending mode was obtained by assuming a power series in η_{Ω} which satisfied

(1) the boundary conditions for a cantilever mount,

(2) the condition of orthogonality with the first bending mode, and

(3) the condition of zero deflection at the 75 percent span location.

Condition (3) was obtained from observation of the node line for the second bending mode of the actual mode during vibration tests.

The parameters used in the analyses were

$\mu_{\Omega} = 30$ $a = -0.20$

$r_{\alpha_{\Omega}}^2 = 0.250$ $\Omega = 43°14'$

$x_{\alpha_{\Omega}} = 0.20$ $\dfrac{d}{b_{\Omega_0}} = 0.66798$

$\dfrac{b_{\Omega_0}}{\ell_{\Omega}} = 0.21233$ $\dfrac{\ell_{\Omega}}{b_{\Omega_0}} \sin \Omega = 3.22603$

which resulted in the following values for the coefficients of the flutter equations.

$$A = 0.078,125\ L_{hh} + 0.025,919\ L_{hh'} + 2.071,439 \left[1 - \left(\frac{\omega_{h_1}}{\omega_{\alpha_1}}\right)^2 Z\right] \quad (43)$$

$$B = 0.020,332\ L_{hh} + 0.051,958\ L_{hh'} \quad (44)$$

$$C = 0.061,035\ L_{h\alpha} + 0.010,799\ L_{h\alpha'} + 0.342,857 \quad (45)$$

$$D = -0.228,066\ L_{hh} + 0.059,291\ L_{h\alpha} + 0.055,743\ L_{hh'} + 6.582,193 \quad (46)$$

$$E = 0.020,331,530\ L_{hh} - 0.000,120,555\ L_{hh'} \quad (47)$$

$$F = 0.091,120\ L_{hh} + 0.025,919\ L_{hh'} + 3.417,742 \left[1 - \left(\omega_{h_2}/\omega_{\alpha_1}\right)^2 Z\right] \quad (48)$$

$$G = -0.000,283,89\ L_{h\alpha} - 0.004,972,8\ L_{h\alpha'} - 0.212,126 \quad (49)$$

$$H = 0.038,584\ L_{hh} - 0.027,302\ L_{h\alpha} - 0.025,668\ L_{hh'} - 1.161,620 \quad (50)$$

$$I = 0.061,035\ M_{\alpha h} + 0.021,599\ M_{\alpha h'} + 0.342,857 \quad (51)$$

$$J = -0.000,283,89\ M_{\alpha h} + 0.037,371\ M_{\alpha h'} - 0.212,126 \quad (52)$$

$$K = 0.050,863\ M_{\alpha\alpha} + 0.010,124\ M_{\alpha\alpha'} + 0.441,964\ [1 - Z] \quad (53)$$

$$L = -0.180,995\ M_{\alpha h} + 0.055,585\ M_{\alpha\alpha} + 0.052,259\ M_{\alpha h'} + 1.691,275 \quad (54)$$

$$M = 0.059,291\ M_{\alpha h} + 0.023,604\ M_{\alpha h'} + 0.228,066\ L_{hh} + 0.076,860\ L_{hh'} + 6.582,193 \quad (55)$$

$$N = -0.027,302\ M_{\alpha h} + 0.023,604\ M_{\alpha h'} + 0.038,584\ L_{hh} + 0.158,271\ L_{hh'} - 1.161,620 \quad (56)$$

$$O = 0.055,585\ M_{\alpha\alpha} + 0.014,753\ M_{\alpha\alpha'} + 0.180,995\ L_{h\alpha} + 0.030,618\ L_{hh'} + 1.691,275 \quad (57)$$

$$P = -0.168,098\ M_{\alpha h} + 0.080,996\ M_{\alpha\alpha} + 0.076,149\ M_{\alpha h'} - 0.687,648\ L_{hh}$$
$$+ 0.168,098\ L_{h\alpha} - 0.156,038\ L_{hh'} + 23.195,949 \left[1 - \left(\frac{\omega_\phi}{\omega_{\alpha_1}}\right)^2 Z\right] \quad (58)$$

3 Solution of Equations of Motion for Flutter

The flutter equations for the swept stabilizer were solved for two (bending-torsion), three (bending-torsion-pitch) and four (first bending-second bending-torsion-pitch) degree-of-freedom systems. The flutter determinants for each system are respectively

$$\begin{vmatrix} A & C \\ I & K \end{vmatrix} = 0$$

$$\begin{vmatrix} A & C & D \\ I & K & L \\ M & O & P \end{vmatrix} = 0$$

$$\begin{vmatrix} A & B & C & D \\ E & F & G & H \\ I & J & K & L \\ M & N & O & P \end{vmatrix} = 0 \qquad (59)$$

where A, B, ----P are given by Eqs. (43) through (58). In each case the aerodynamic terms were evaluated by selecting specific combinations of M and k.

The general pattern of solution of the three flutter determinants was the same. A given determinant was first expanded into a complex polynomial. Since the right-hand side of the equation was zero, two separate equations were written by setting both the real and imaginary parts of the polynomial equal to zero. These two simultaneous equations were solved for any two desired eigenvalues.

In the two-degree-of-freedom case, the complex polynomial resulting from the expansion of the determinant was solved for the eigenvalues $(\omega_{h_1}/\omega_{\alpha_1})^2$ and $(\omega_{\alpha_1}/\omega_f)^2$. The cross flow Mach numbers used were $M_\Omega = 0$, 10/9, 5/4 and 10/7. This case corresponds to the pitch-locked condition.

The three-degree-of-freedom system was solved for the two eigenvalues $(\omega_\phi/\omega_f)^2$ and $(\omega_{\alpha_1}/\omega_f)^2$. $(\omega_{h_1}/\omega_{\alpha_1})^2$ was set equal to 0.0625, a value which corresponded closely to the average value for the actual stabilizer models. Again $M_\Omega = 0$, 10/9, 5/4, and 10/7 were used.

Finally, for the four-degree-of-freedom systems, $Z = (\omega_{\alpha_1}/\omega_f)^2 (1 + ig)$ was used as the eigenvalue. Here, it was necessary to specify values of $(\omega_{h_1}/\omega_{\alpha_1})^2$, $(\omega_{h_2}/\omega_{\alpha_1})^2$ and $(\omega_\phi/\omega_{\alpha_1})^2$ in advance. The solutions of the fourth-order determinants were carried out on a 650 IBM computer using a program developed by North American Aviation in Columbus, Ohio, and the results plotted on a

V-g diagram. Value of the constants for which solutions were found were $(\omega_{h_1}/\omega_{\alpha_1})^2 = 0.0625$, $(\omega_{h_2}/\omega_{\alpha_1})^2 = 0.9025$, 1.155625 for $(\omega_\phi/\omega_{\alpha_1})^2 = 0.30$ and $(\omega_{h_1}/\omega_{\alpha_1})^2 = 0.0625$, $(\omega_{h_2}/\omega_{\alpha_1})^2 = 1.155625$ for $(\omega_\phi/\omega_{\alpha_1})^2 = 0.20$.

The results from the two- and three-degree-of-freedom cases are plotted in Fig. 9 and then crossplotted in Fig. 1. The pitch-locked values shown as asymptotes as $(\omega_\phi/\omega_{h_1})^2 \to \infty$ in Fig. 9 and as the $(\omega_\phi/\omega_{h_1})^2 \to \infty$ boundary in Fig. 1 are the results of the two-degree-of-freedom calculations.

The most interesting feature of these analyses are the very deep "buckets" that occur at low values of $(\omega_\phi/\omega_{h_1})^2$ in Fig. 9 and correspondingly at low values of $(\omega_\phi/\omega_{\alpha_1})^2$ in Fig. 1. In some cases the curves actually double back on themselves giving two regions of stability at a given value of $(\omega_\phi/\omega_{h_1})^2$ or Mach number. The presence of these "buckets" is apparently due to a change in flutter mode shape and can be explained by looking at sample four-degree-of-freedom calculations in some detail.

Each solution for the four-degree-of-freedom problem at a given set of values for $(\omega_{h_1}/\omega_{\alpha_1})^2$, $(\omega_{h_2}/\omega_{\alpha_1})^2$, and $(\omega_\phi/\omega_{\alpha_1})^2$ and Mach number, yields four separate curves on branches on a V-g plot and several values of k for the flutter condition of g = 0 (see Fig. 10). Since each branch represents a particular mode of flutter, it appears from Fig. 10 at $M_\Omega = 10/9$ (M = 1.525) that the stabilizer is capable of flutter in the 1st mode and the 2nd mode. At $M_\Omega = 5/4$ (M = 1.716) the stabilizer has one unstable region along the V axis in the 2nd mode and two unstable regions in the 3rd mode. A set of three-dimensional sketches of V versus g versus M is shown in Fig. 11. To avoid confusion, each sketch contains only one type of flutter mode. Because of the difficulty in following the various possible flutter modes from a V-g diagram to a $V_f/\omega_{\alpha_1} b_{0.75}$ versus M plot, the results of the four-degree-of-freedom analysis of Fig. 12 were ultimately drawn after looking at three-dimensional plots of V versus g versus M with interest concentrated on the traces of the different modes in the g = 0 plane.

The lowest set of curves on $V_f/\omega_{\alpha_1} b_{0.75}$ versus M in Fig. 12 form the critical flutter boundary. This boundary, as can be seen by looking at Fig. 12 is formed by three different flutter modes each becoming the critical boundary of instability over a particular Mach number range. The flutter boundary from the four-degree-of-freedom analysis for $(\omega_\phi/\omega_{\alpha_1})^2 = 0.30$ appears to compare

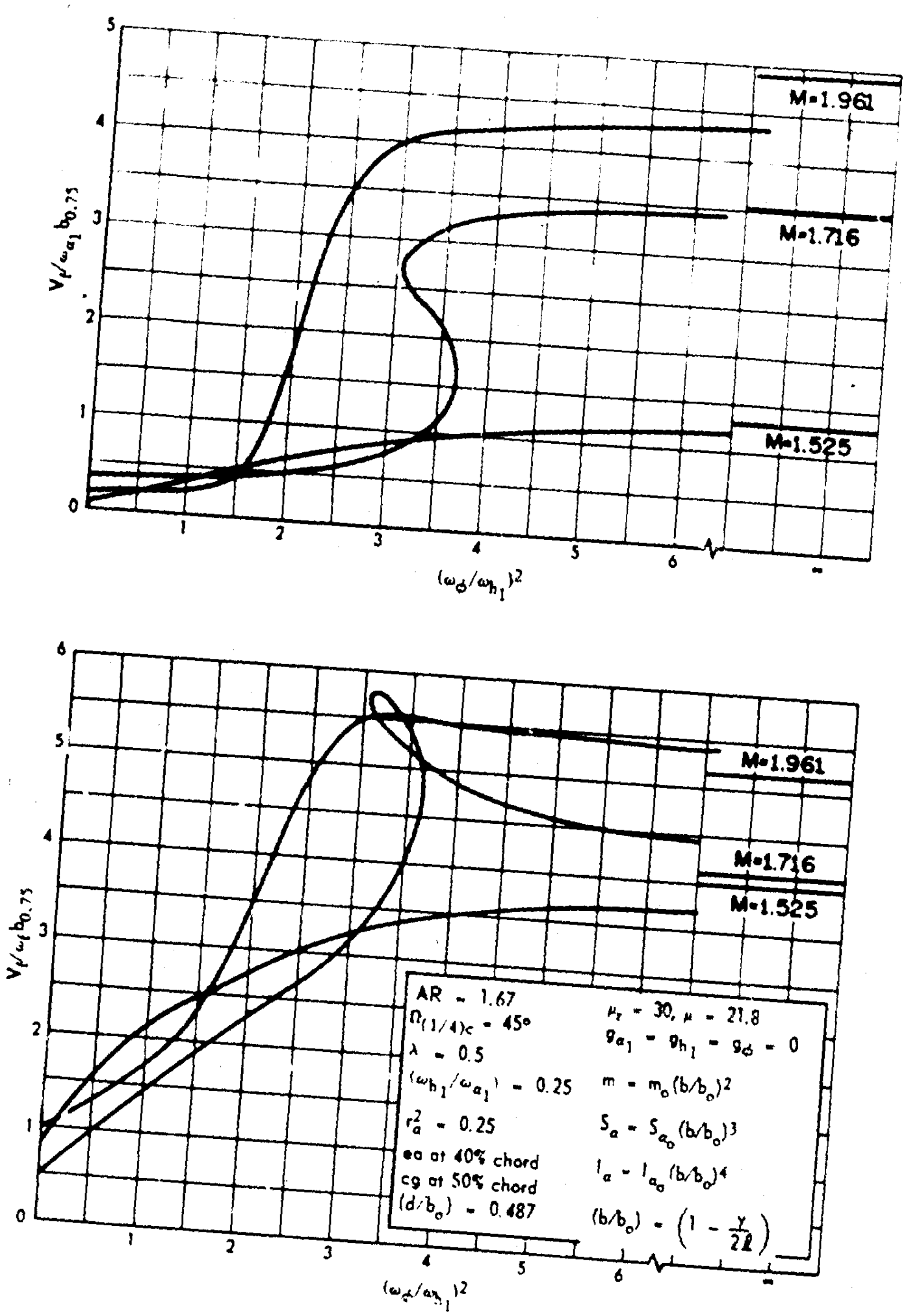

Fig. 9. Flutter parameters $V_f/\omega_{a_1} b_{0.75}$ and $V_f/\omega_f b_{0.75}$ versus $(\omega_\phi/\omega_{h_1})^2$ from two- and three-degree-of-freedom calculations.

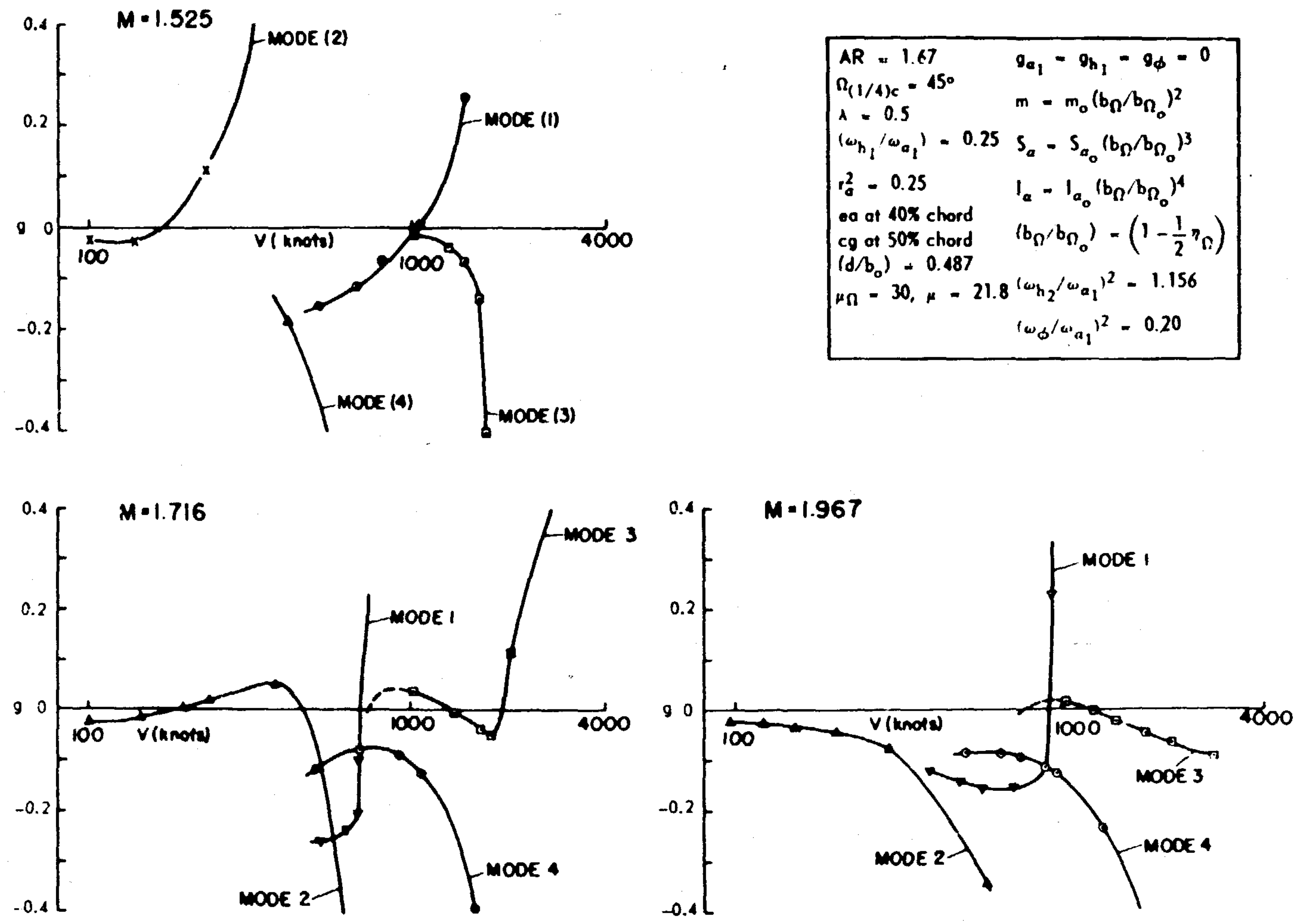

Fig. 10. V-g curves from four-degree-of-freedom calculations.

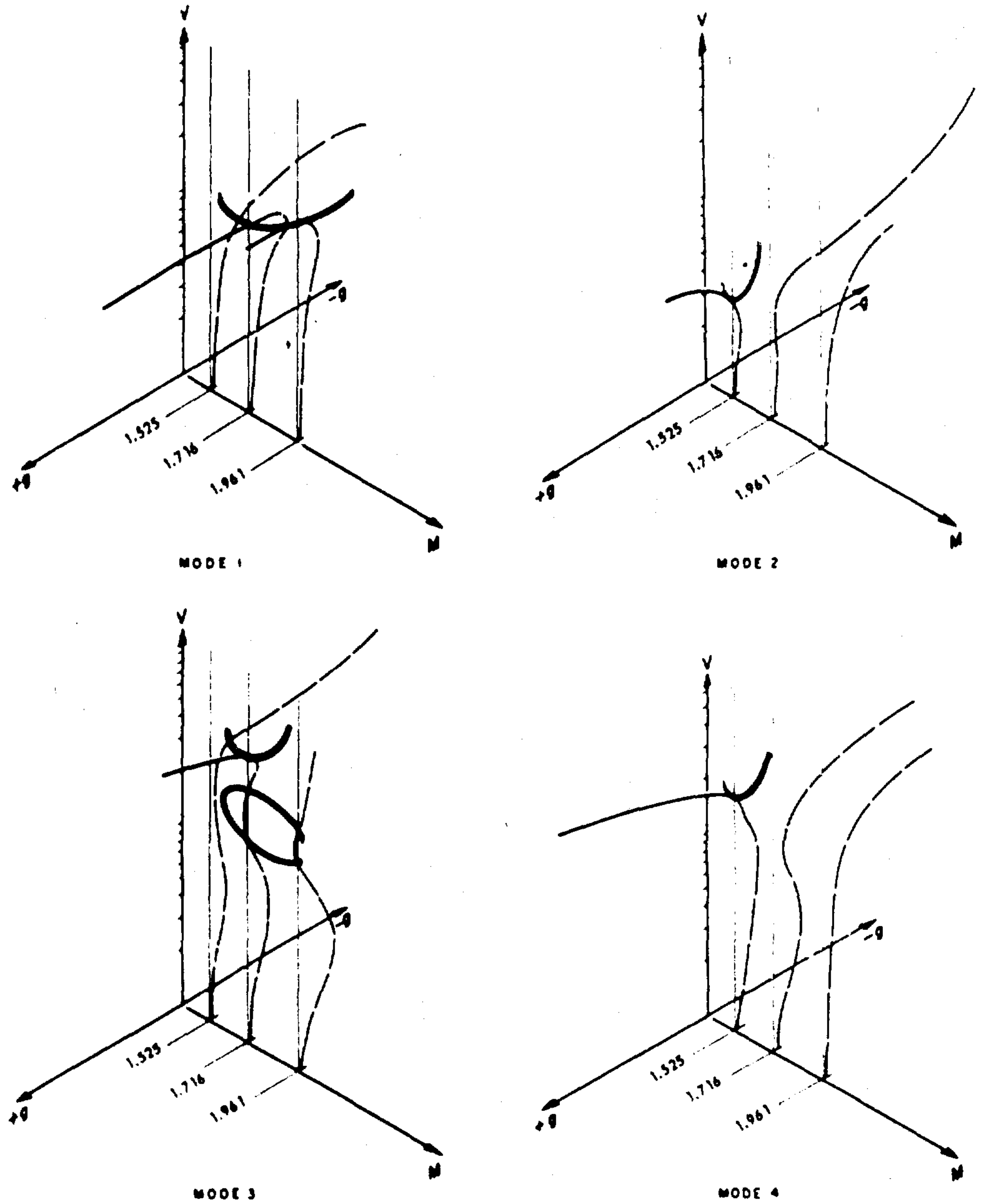

Fig. 11. Sketches of V versus g versus Mach number curves from four-degree-of-freedom calculations.

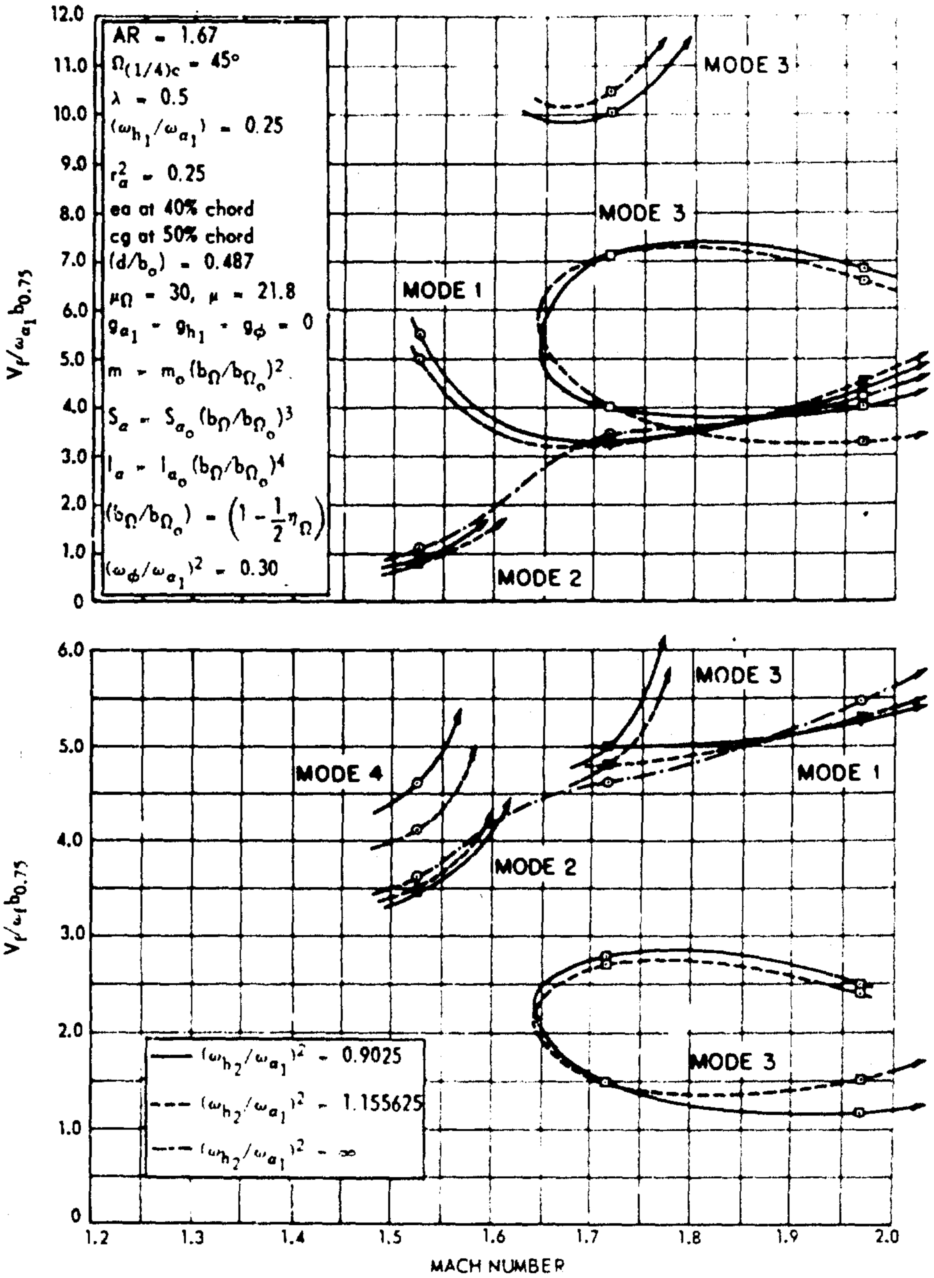

Fig. 12. Flutter parameters $V_f/\omega_{a_1} b_{0.75}$ and $V_f/\omega_f b_{0.75}$ versus Mach number from four-degree-of-freedom calculations.

very favorably with the three-degree-of-freedom flutter boundary $\left[(\omega_{h_2}/\omega_{\alpha_1})^2 = \infty\right]$ which is also shown in Fig. 12. Thus, the second-bending degree of freedom apparently has little influence on the flutter parameter $\dfrac{V_f}{\omega_{\alpha_1} b_{0.75}}$ of a swept stabilizer below M = 2.0 except for a general lowering of the curve. In using the four-degree-of-freedom analysis to interpret the points found in the three-degree-of-freedom analysis, it is seen that the S-shaped curves of Fig. 9 do indeed appear reasonable and are a direct result of a change in critical flutter modes in going from low Mach number to high Mach number.

Another interesting characteristic of the V-g solutions of the four-degree-of-freedom analysis is the variation in the flutter boundary with small changes in the structural damping coefficient, "g." By referring to Fig. 13, it is seen that increasing the structural damping from g = 0 to g = 0.06 moves the "bucket" on the flutter boundary due to the 2nd mode from about M = 1.75 to about M = 1.65. The general level of the flutter boundary as determined by the 1st and 2nd modes will not be changed.

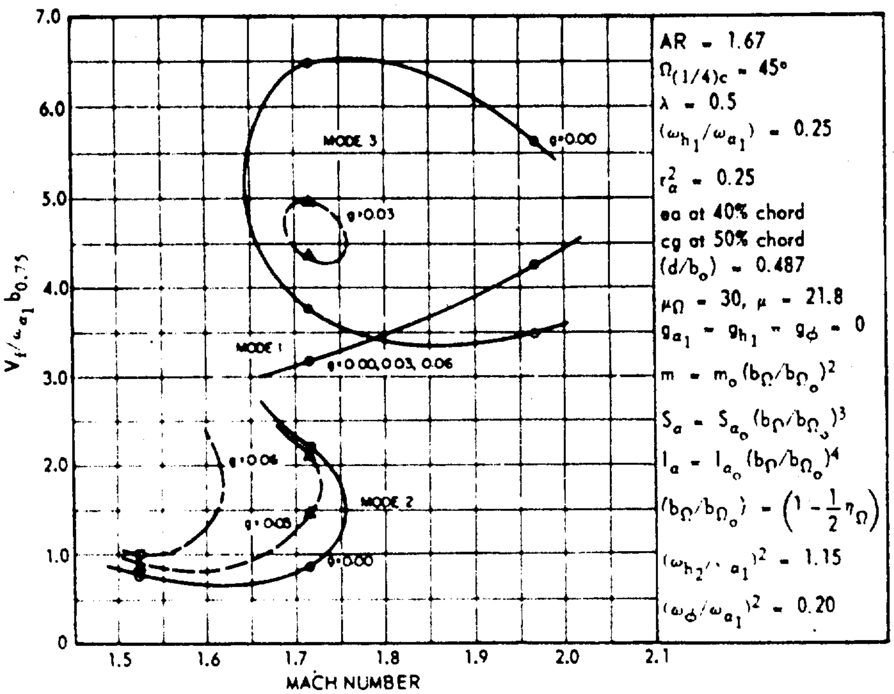

Fig. 13. Variation of $V_f/\omega_{\alpha_1} b_{0.75}$ versus Mach number with change in structural damping from four-degree-of-freedom calculations.

APPENDIX II

EXPERIMENTAL DATA

This appendix gives the detailed tabulation of both design and experimental data. Since both the model design and the testing techniques are essentially the same as those described in Ref. 2, little discussion of them is included in this appendix.

The planform of the stabilizer models is shown in Fig. 14a and a cross section of the root of the SWS-1 series models is shown in Fig. 14b. Root cross sections for the SWS-2 and the SWS-3 series models are not shown since they differ only in minor details from the SWS-1 model. As can be seen in Fig. 14b the spar, which contributes essentially all of the model bending stiffness and most of the torsional stiffness, is constructed of a pine core around which is wrapped an aluminum skin. Steel caps are then cemented to the spar. Both the steel and aluminum are tapered linearly along the span giving, when combined with the taper of the height and width of spar, the required fourth-power distribution to the bending and torsional rigidities, EI_{Ω} and GJ_{Ω} :

$$EI_{\Omega} = EI_{\Omega_o}\left(\frac{b_{\Omega}}{b_{\Omega_o}}\right)^4 \tag{60}$$

$$GJ_{\Omega} = GJ_{\Omega_o}\left(\frac{b_{\Omega}}{b_{\Omega_o}}\right)^4 \tag{61}$$

where

$$\left(\frac{b_{\Omega}}{b_{\Omega_o}}\right) = (1 - y/2\ell) \tag{62}$$

Balsa wood cemented to the spar was used to give the aerodynamic shape required, and suitably spaced lead weights were used to give the mass parameters required. Table 1 gives a summary of the design parameters for all of the stabilizer models.

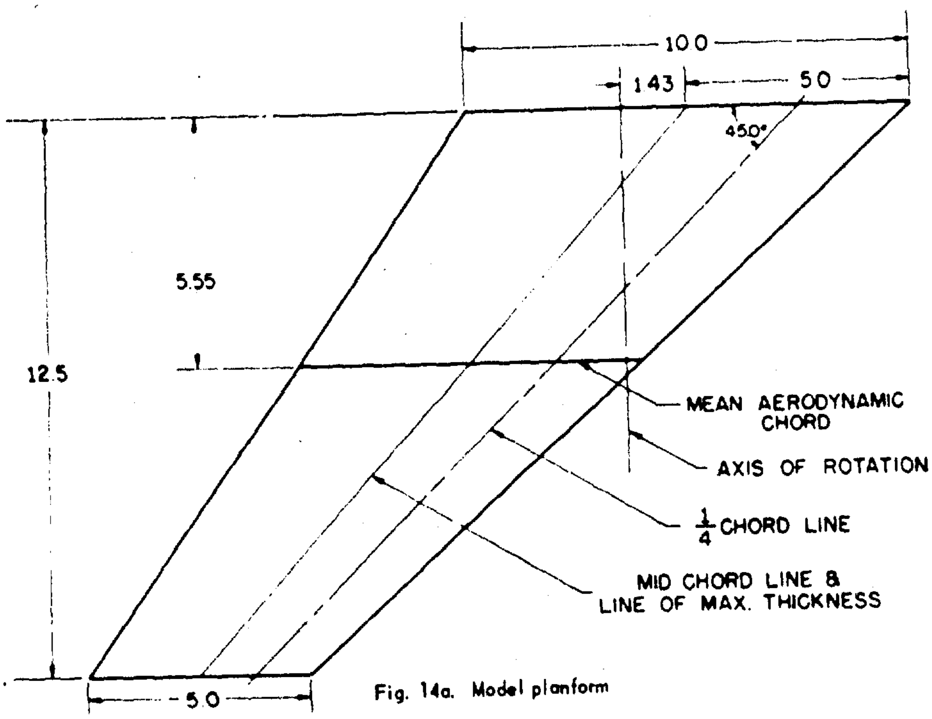

Fig. 14a. Model planform

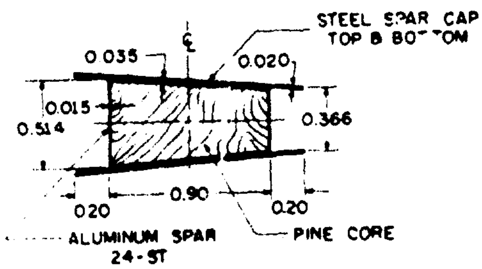

SPAR CROSS-SECTION DETAIL AT ROOT

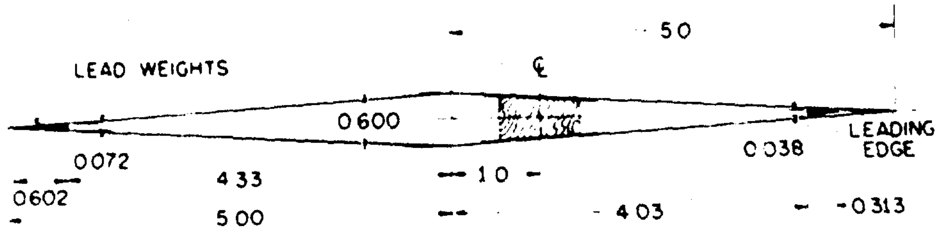

Fig. 14b. Model cross-section detail at root

Fig. 14. Swept stabilizer design drawings (all dimensions in inches).

Table 1. Design parameters for swept stabilizer models.

The parameters presented in this table are common to all the models built in this program.	
Geometric Parameters	
Panel aspect ratio, AR	1-2/3
Taper ratio, λ	1/2
Sweep angle of 1/4 chord,	45.0°
Mean aerodynamic chord (in.), MAC	7.7778
Section max. thickness (% chord),	6.0%
Line of max. thickness (% chord)	50.0%
Design Parameters	
Section center of gravity location (% chord), (cg)	50.0%
Radius of gyration (fraction of semichord), r_α	0.50
Calculated locus of shear centers (% chord), (ea)	40.0%
Properties of Balsa Wood (average values)	
Modulus of elasticity in bending (lb/in^2), E	6400
Modulus of elasticity in torsion (lb/in^2), G	20,000
Density (lb/in^3), ρ_{BA}	0.003900
Properties of Pine Core	
Modulus of elasticity in bending (lb/in^2), E	1.329×10^6
Modulus of elasticity in torsion (lb/in^2), G	0.107×10^6
Density (lb/in^3), ρ_p	0.014

The root fitting and the mounting block with the pitching mechanism are shown in Fig. 15. The spar was glued and screwed to the root fitting, shown removed from the mounting in Fig. 15a. Pitching frequency was controlled by changing the thickness of the flexure shown on the end of the root fitting in Fig. 15a. Figure 15b shows the rear of the mounting block with the flexure in place. The angle of attack of the model could be changed by rotating the whole clamp shown in Fig. 15b. Drag and lift loads were carried adequately by three ball bearings in the mounting block. The gap between the root and the mounting block was sealed with aluminum foil for all tests.

With the pitching mechanism "locked out," static tests were made on most of the models in an attempt to determine the cantilever properties of the model. The properties determined were measured elastic axis, $(ea)_M$, as discussed in Ref. 2, and the root values of EI_Ω and GJ_Ω. The results of these measurements are given in Table 2. There is considerable scatter in the EI_Ω, GJ_Ω and $(ea)_M$ data.

The measured mass per unit length at the root $(mo)_M$ is also given in Table 2. This quantity was indirectly measured using the assumed mass distribution

$$m(y) = (m_o)_M \left(1 - \frac{y}{2\ell}\right)^2 \qquad (63)$$

By just measuring the total mass and then computing $(m_o)_M$ from

$$(m_o)_M = \frac{\text{total mass}}{\int_o^\ell \left(1 - \frac{y}{2\ell}\right)^2 dy} \qquad (64)$$

Fig. 15a.

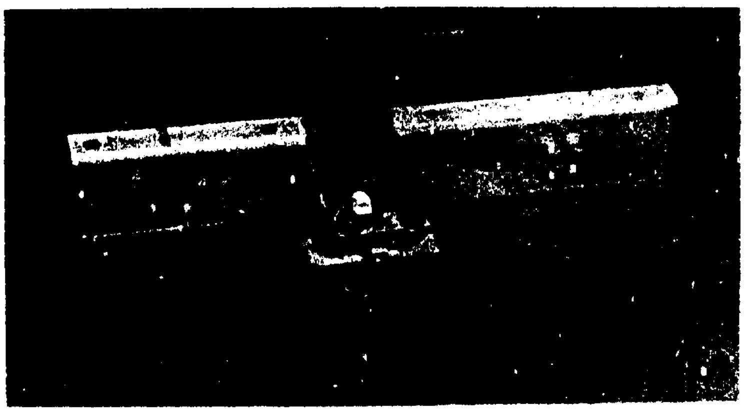

Fig. 15b.

Fig. 15. Pictures of root mounting block.

In Eq. (64) the total mass does not include the mass of the root fitting, so that the value for $(m_o)_M$ includes only the mass of the balsa, lead, glue and the spar.

Data for the pitching frequency is found in Table 3. The mass moment of inertia of the whole model, including the root fitting, was obtained by swinging the model with a bifilar pendulum. The pitching mechanism flexibility influence coefficients, C_ϕ, was measured with a transit and mirror arrangement. The pitching frequency was then calculated as:

$$f_\phi = \frac{1}{2\pi} \sqrt{\frac{1}{I_\phi \ C_\phi}} \tag{65}$$

The results of the flutter tests are given in Table 4. For the sake of convenience, most of the important experimental natural still-air-vibration frequencies are included as well as the tunnel conditions at flutter. If flutter occurred, the conditions at the start of flutter are given. If no flutter occurred during the test run, the conditions at the start and end of the test are given. Figures 16 and 17 are excerpts from the high speed movies taken during the flutter of the SWS-1-98 and the SWS-3d-87 models, respectively. These portions of the movies have been analyzed and the results are presented in terms of the pitching motion at the root and the motion of the tip sections in Figs. 18 and 19. These flutter modes are typical of those encountered for the stabilizer models.

Complete vibration data, including sketches of node lines, frequency, and structural damping of the lower modes of vibration are found in Table 5. All of the models were vibration tested in both the "locked," or cantilever, condition and with the pitching mechanism in. Figure 20 is a plot of the normalized coupled frequencies with the pitching mechanism in. The lowest cantilever bending frequency, f_{hN}, was used as the normalizing frequency. It is interesting to note that the frequencies of the first coupled modes, f_1, for most of the stabilizer models fall along a common curve with not too much scatter. The same is true for the frequencies of the second coupled mode, f_2.

Table 6 gives the influence coefficient data for the models with the pitching mechanism in and Fig. 21 shows the location of the stations at which influence coefficients were taken.

Table 2. Static data for swept stabilizer models.

Model	$(m_o)_M$ (slug/ft)	$(ec)_M$ (% chord)	$(GJ_{o\Omega})_M$	$(EI_{o\Omega})_M$
SWS-1	0.0214		3.690×10^4	8.493×10^4
SWS-2	0.0214		2.696×10^4*	6.860×10^4*
SWS-1b	0.0220		2.877×10^4	6.661×10^4
SWS-1c	0.0225	46.5%	3.459×10^4	7.422×10^4
SWS-1d	0.0225	49.0%	2.380×10^4	5.84×10^4
SWS-1e	0.0246	39.0%	4.220×10^4	7.836×10^4
SWS-3	0.0240	35.36%	7.572×10^4	10.448×10^4
SWS-3a	0.0231	43.0%	3.680×10^4	8.59×10^4
SWS-3b	0.0224	50%	5.23×10^4	7.139×10^4
SWS-3c	0.0233		1.942×10^4*	6.754×10^4*
SWS-3d	0.0247	50%	5.234×10^4	7.489×10^4
SWS-3e	0.0274		3.89×10^4*	8.89×10^4*

* Data for spar only.

Table 3. Pitching frequency data.

Model	$(I_\phi)_{meas}$ (slug-ft^2)	$(C_\phi)_{meas}$ (rad/lb-ft)	f_ϕ (cps)
SWS-1-L	0.00244	0.000022	
SWS-1-138	0.00244	0.000543	138
SWS-1-105	0.00244	0.000915	105
SWS-1-98	0.00244	0.001072	98.3
SWS-2-L		0.000022	
SWS-1b-L	0.00223	0.000022	
SWS-1c-48	0.00238	0.004460	47.6
SWS-1d-L		0.000032	
SWS-1e-74	0.00226	0.002132	73.7
SWS-3-53	0.00206	0.004460	52.5
SWS-3a-63	0.00224	0.002854	63.1
SWS-3b-53	0.00212	0.004249	53.0
SWS-3c-74	0.00205	0.00224	74.4
SWS-3d-87	0.00225	0.001498	86.7
SWS-3e-120	0.00275	0.000628	120.0

Table 4. Experimental flutter data.

Model	M_f	f_f (cps)	V_f ft/sec	μ_f	$\frac{V_f}{b_{0.75}\omega_{\alpha_n}}$	$\frac{V_f}{b_{0.75}\omega_f}$	$\frac{b_{0.75}\omega_1}{a_f}\sqrt{\frac{\mu_f}{65}}$	$\frac{b_{0.75}\omega_2}{a_f}\sqrt{\frac{\mu_f}{65}}$	f_{h_N} (cps)	f_{α_N} (cps)	f_ϕ (cps)	$\frac{f_1}{f_{h_N}}$	$\frac{f_2}{f_{h_N}}$	$\frac{f_3}{f_{h_N}}$	$\frac{f_\phi}{f_{\alpha_N}}$	g_{av} Modes 1 & 2	Remarks
SWS-1 Locked	1.98 – 1.56		1659 – 1427	33.1 – 22.1			0.090 – 0.068	0.299 –0.226	64.5	214	∞	1.00	3.32	3.71	∞	0.018	Run 1 No flutter
SWS-1 Locked	1.65 – 1.35		1483 – 1292	29.6 – 22.6			0.079 – 0.065	0.262 – 0.216	64.5	214	∞	1.00	3.32	3.71	∞	0.018	Run 2 No flutter.
SWS-1 138	1.98 – 1.56		1670 – 1431	33.7 – 22.3			0.073 – 0.055	0.296 – 0.224	64.5	214	138	0.81	3.29	3.33	0.645	0.04	Run 1 No flutter
SWS-1 138	1.65 – 1.35		1486 – 1289	30.0 – 22.3			0.065 – 0.053	0.263 – 0.212	64.5	214	138	0.81	3.29	3.33	0.645	0.04	Run 2 No flutter
SWS-1 105	1.98 – 1.55		1657 – 1416	33.0 – 21.7			0.074 – 0.055	0.275 – 0.206	64.5	214	105	0.82	3.07	3.35	0.491	0.032	Run 1 No flutter
SWS-1 105	1.65 – 1.35		1490 – 1280	29.8 – 21.7			0.065 – 0.053	0.246 – 0.198	64.5	214	105	0.82	3.07	3.35	0.491	0.032	Run 2 No flutter
SWS-1 98	1.97 – 1.56		1642 – 1421	32.2 – 22.1			0.069 – 0.053	0.252 – 0.193	64.5	214	98.3	0.78	2.84	3.19	0.459	--	Run 1 No flutter
SWS-1 98	1.35	107	1280	22.3	3.65	7.32	0.051	0.188	64.5	214	98.3	0.78	2.84	3.19	0.459	--	Run 2 Model fluttered
SWS-1b Locked	1.98 – 1.56		1655 – 1420	33.9 – 22.7			0.075 – 0.056	0.285 – 0.214	52.8	202	∞	1.00	3.83	4.13	∞	0.024	No flutter for Runs 1 and 2
SWS-1b Locked	1.65 – 1.35		1480 – 1285	31.0 – 24.0			0.067 – 0.055	0.254 – 0.211	52.8	202	∞	1.00	3.83	4.13	∞	0.024	Model with flexure, SWS-1b-142, destroyed by starting shock
* SWS-1c 48	1.98	97	1665	34.4	4.74	10.47	0.060	0.240	60.0	214	47.6	0.71	2.82	3.33	0.220	0.04	Injection flutter
SWS-1d Locked	1.74	127	1555	26.9	5.68	7.47	0.070	0.197	59.1	167	∞	1.00	2.82	3.29	∞	0.023	Retraction flutter Tip damaged on injection
SWS-1e 74	1.58	132	1450	27.5	4.42	6.70	0.054	0.199	62.0	200	73.7	0.75	2.77	3.42	0.368	0.015	Model fluttered
SWS-2 Locked	1.55	150	1420	21.3	4.32	5.76	0.053	0.204	52.0	200	∞	1.00	3.85	4.02	∞	0.029	Retraction flutter
SWS-3 53	2.06 – 1.8		1720 – 1580	38.6 – 30.2			0.065 – 0.057	0.302 – 0.265	68.8	291	52.5	0.65	3.05	3.52	0.180	0.044	No flutter, model destroyed at M = 1.80
* SWS-3a 63	2.06	100	1710	37.4	3.61	10.46	0.073	0.305	66.7	290	63.1	0.73	3.06	3.68	0.218	0.017	Injection flutter
* SWS-3b 53	2.07	108	1705	35.8	3.48	9.66	0.061	0.282	67.3	300	53.0	0.62	2.85	3.34	0.177	0.026	Injection flutter
SWS-3c 74	2.05	110	1700	33.7	3.47	9.47	0.071	0.283	70.9	300	74.4	0.71	2.82	3.20	0.248	0.024	Flutter with model fully in but Mach number not changed
SWS-3d 87	1.935	122.2	1650	34.9	3.67	8.25	0.0743	0.307	65.6	275	86.7	0.83	3.43	3.72	0.315	0.028	Model fluttered
SWS-3e 120	1.965 – 1.25		1675 – 1240	42.4 – 22.0			0.089 – 0.056	0.383(1) – 0.238	68.0	290	120.0	0.846	3.44	3.64	0.414	0.020	No flutter, third coupled frequency used for $\frac{b_{0.75}\omega_2}{a_f}\sqrt{\left(\frac{\mu}{65}\right)_f}$

(1) Third natural frequency used for parameter.
* Injection flutter

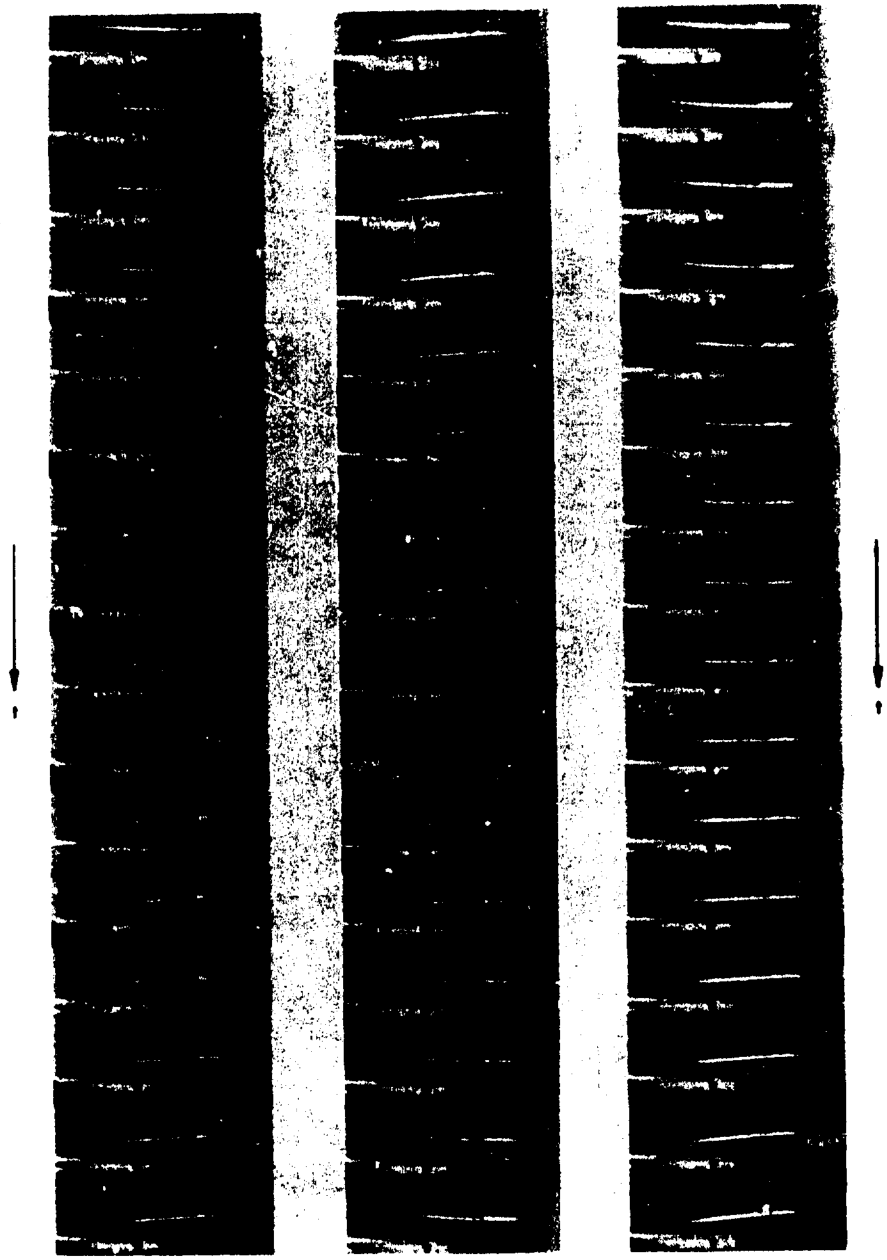

Fig. 16. Pictures of flutter of SWS-1-98 model from high speed movie

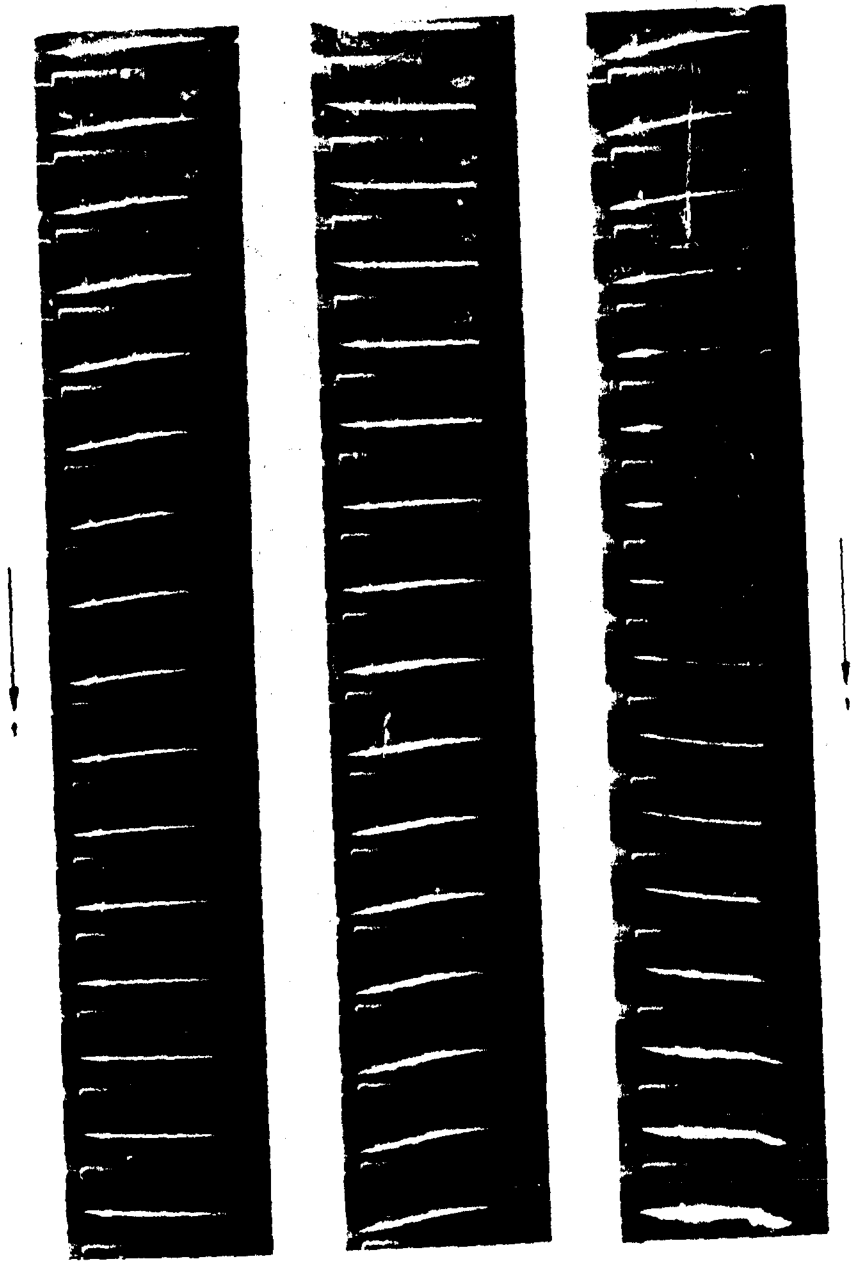

Fig. 17. Pictures of flutter of SWS-3d-87 model from high speed movie.

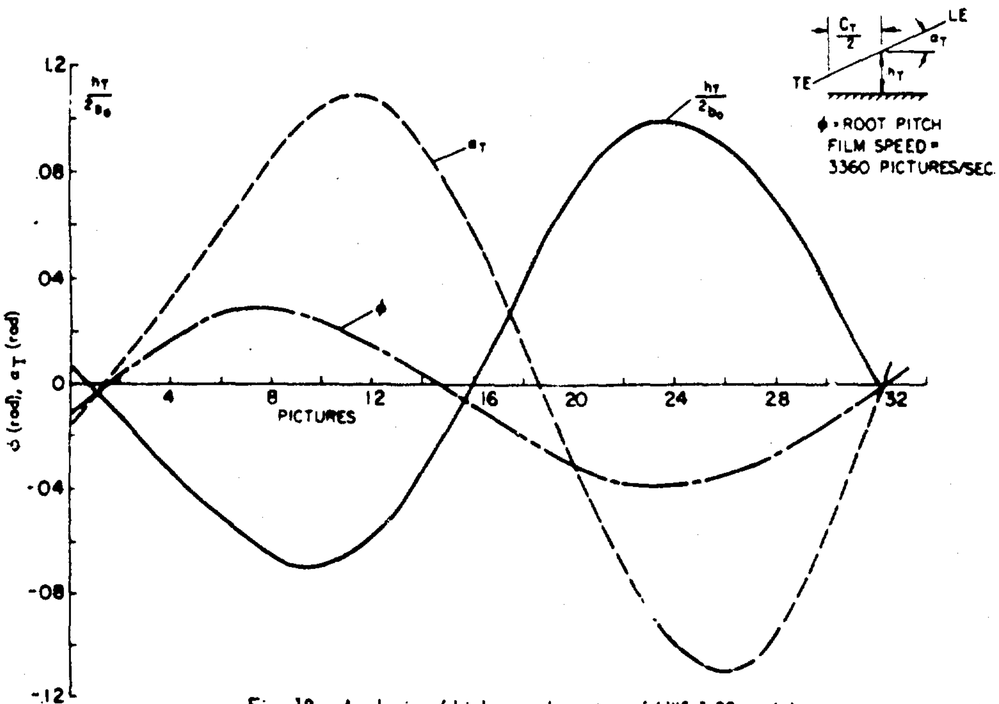

Fig. 18. Analysis of high speed movies of SWS-1-98 model.

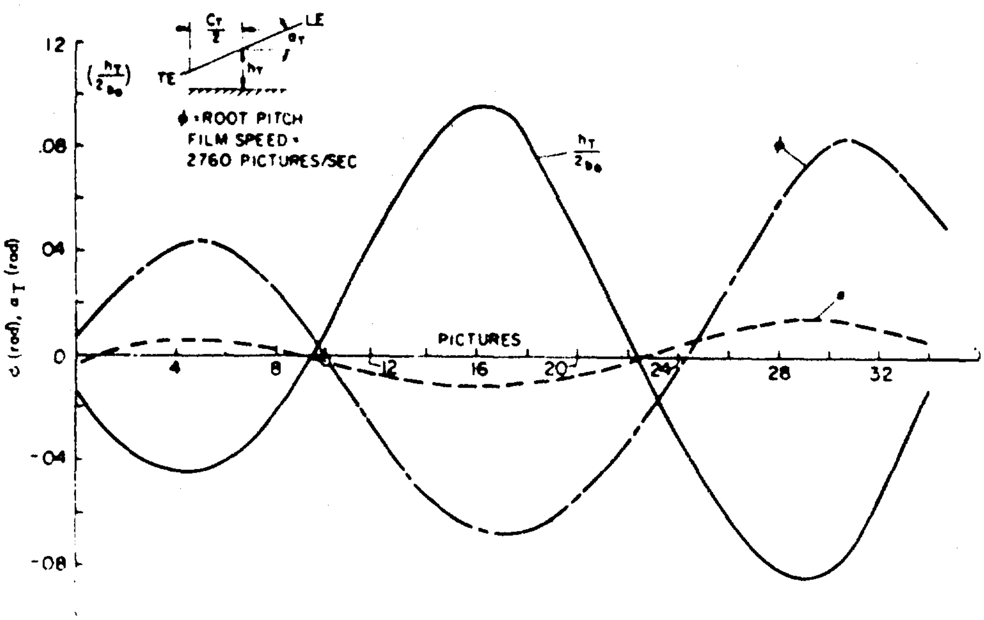

Fig 19. Analysis of high speed movies of SWS-3d-87 model.

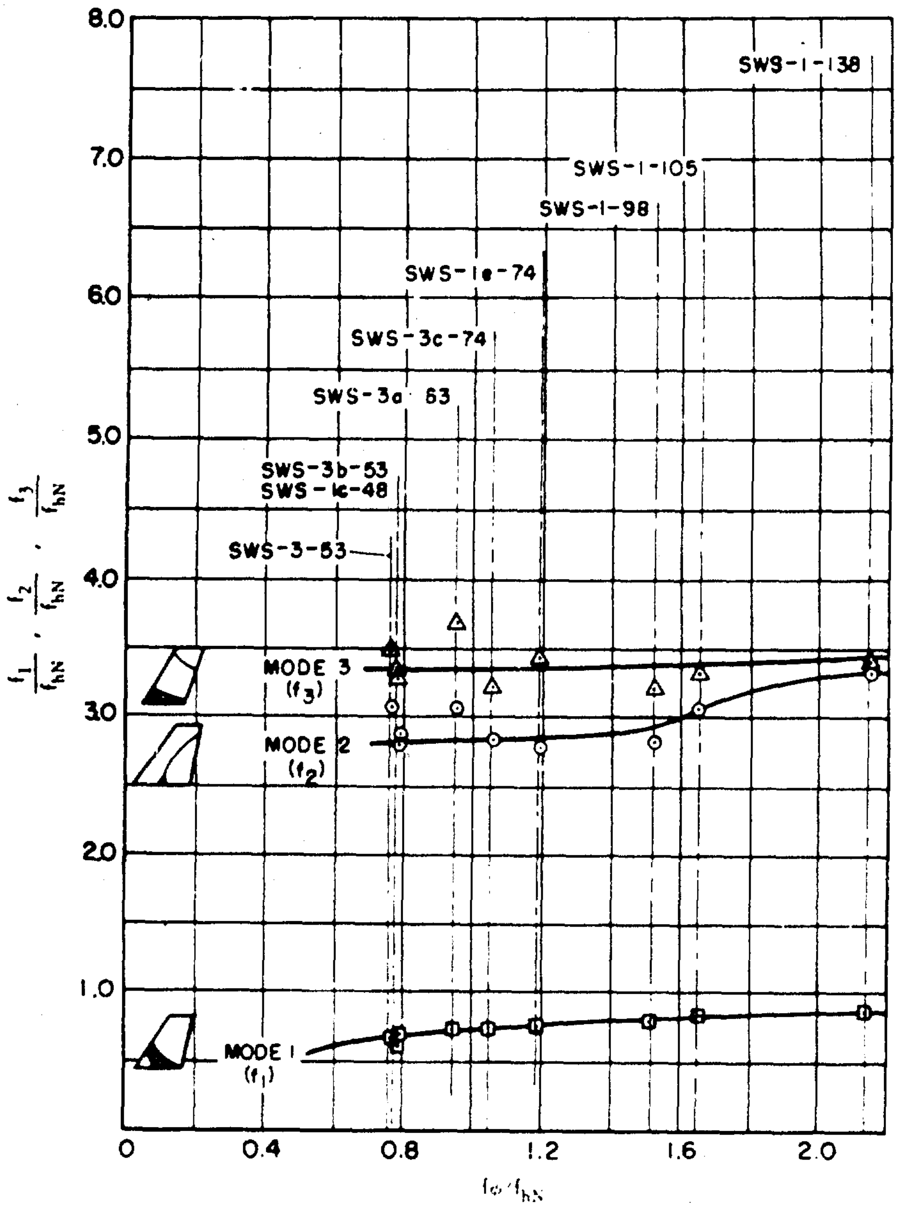

Fig 20 Vibration frequency data for swept stabilizer models

CONFIDENTIAL

AD 142088

Armed Services Technical Information Agency

ARLINGTON HALL STATION
ARLINGTON 12 VIRGINIA

FOR
MICRO-CARD
CONTROL ONLY

2 OF 2

CONFIDENTIAL

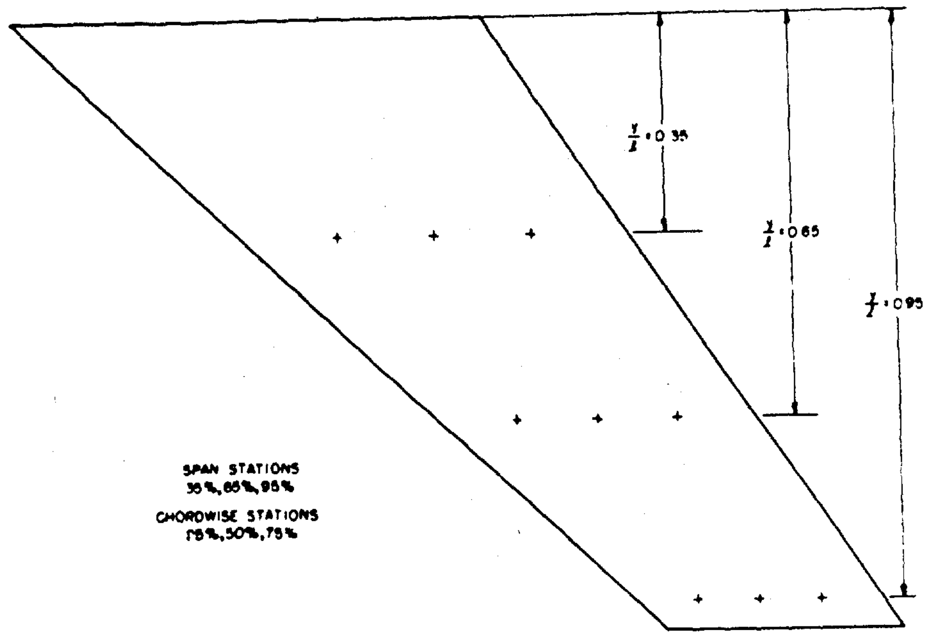

Fig. 21. Location of influence coefficient stations.

Table 5. Experimental vibration data.

MODE / MODEL	FIRST f (cps)	FIRST g	SECOND f	SECOND g	THIRD f	THIRD g	FOURTH f	FOURTH g	UNCOUPLED PITCH f	UNCOUPLED PITCH g
SWS-I LOCKED	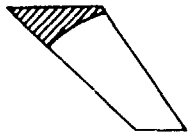 64.5	0.022	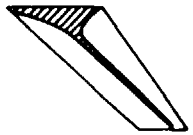 214	0.015	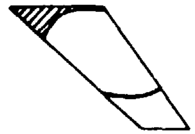 239	—	NONE		LOCKED	
SWS-I -138	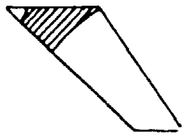 52.4	0.040	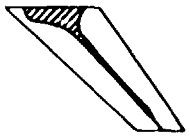 212	—	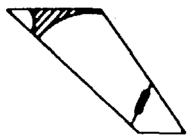 215	0.037	NONE		138	
SWS-I -105	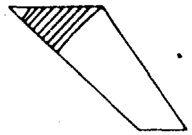 52.9	0.040	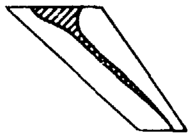 198	0.024	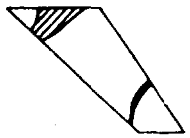 216	0.016	NONE		105	
SWS-I -98	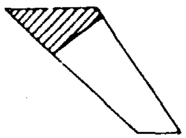 50	—	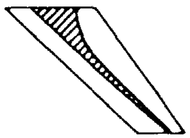 183	—	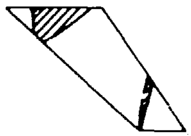 206	—	NONE		98.3	

Table 5. Experimental vibration data. (cont.)

MODEL \ MODE	FIRST f (cps)	FIRST g	SECOND f	SECOND g	THIRD f	THIRD g	FOURTH f	FOURTH g	UNCOUPLED PITCH f	UNCOUPLED PITCH g
SWS – Ib LOCKED	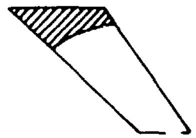 52.8	0.026	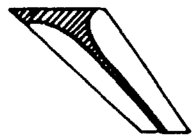 202	0.022	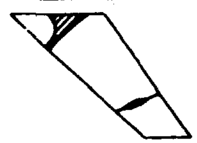 218	0.016	NONE		LOCKED	
SWS – Ib –142	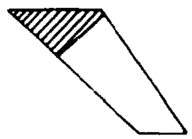 50.0	0.026	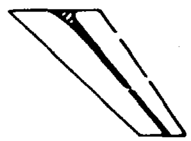 200	0.016	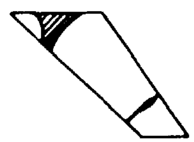 210	0.020	NONE		142	
SWS – Ic LOCKED	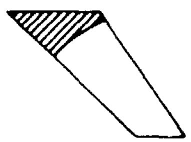 60	—	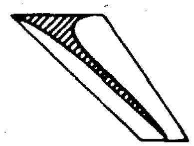 214	—	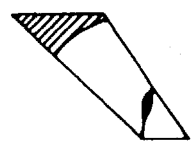 216	—	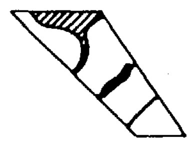 421	—	LOCKED	
SWS – Ic –48	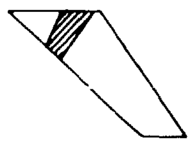 42.3	—	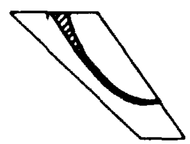 169	0.040	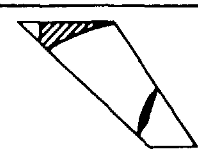 200	0.020	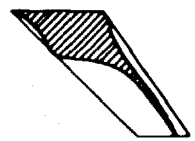 229	0.010	47.6	

Table 5. Experimental vibration data. (cont.)

MODEL \ MODE	FIRST		SECOND		THIRD		FOURTH		UNCOUPLED PITCH	
	f (cps)	g	f	g	f	g	f	g	f	g
SWS-Id LOCKED	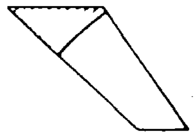 59.1	0.023	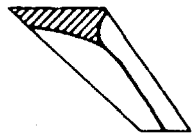 167	—	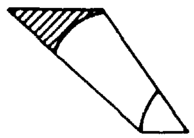 194	0.044	NONE		LOCKED	
SWS-Ie LOCKED	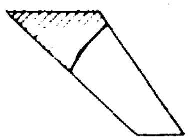 62	—	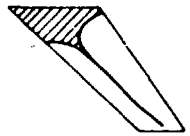 200	0.012	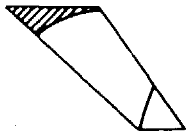 216	0.014	NONE		LOCKED	
SWS-Ie -74	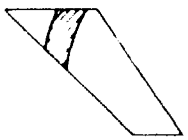 46.6	0.021	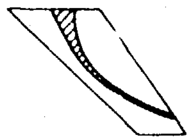 172	0.010	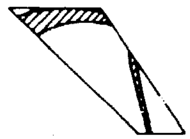 212	0.014	NONE		73.7	
SWS-2 LOCKED	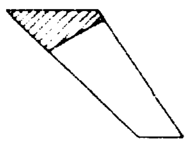 52	0.029	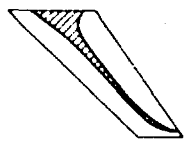 200	—	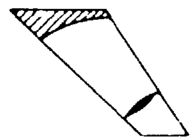 209	0.013	NONE		LOCKED	

Table 5. Experimental vibration data. (cont.)

MODE / MODEL	FIRST f (cps)	FIRST g	SECOND f	SECOND g	THIRD f	THIRD g	FOURTH f	FOURTH g	UNCOUPLED PITCH f	UNCOUPLED PITCH g
SWS-3 LOCKED	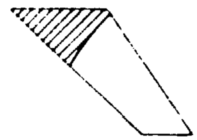 68.8	0.018	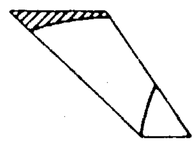 251	—	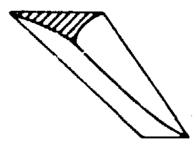 291	—	NONE		LOCKED	
SWS-3 -53	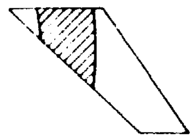 45.0	044	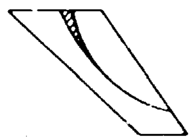 210	—	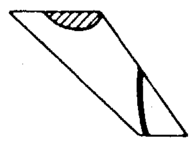 242	0.03	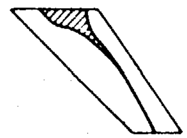 283	—	52.5	
SWS-3a LOCKED	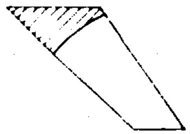 65.7	0.013	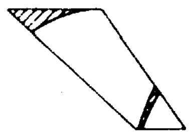 250	0.012	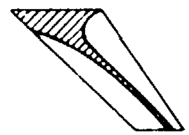 286	0.012	NONE		LOCKED	
SWS-3a 63	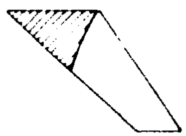 48.4	0.015	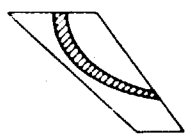 204.2	0.019	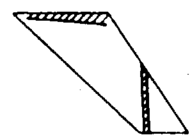 245.5	0.015	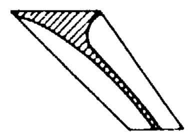 283.3	0.011	63.1	

Table 5. Experimental vibration data. (cont.)

MODE / MODEL	FIRST			SECOND			THIRD			FOURTH			UNCOUPLED PITCH	
		f (cps)	g		f	g		f	g		f	g	f	g
SWS-3b LOCKED	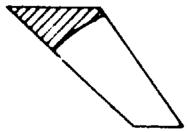	67.3	0.013	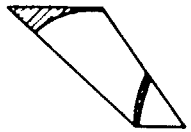	275	0.009	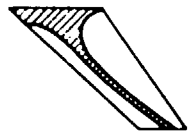	300	—	NONE			LOCKED	
SWS-3b 53	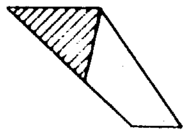	42.1	0.022	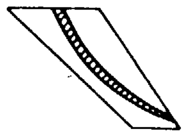	192	0.03	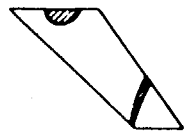	225	0.03	NONE			53.0	
SWS-3c LOCKED	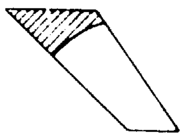	70.9	0.011	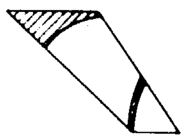	261.5	0.009	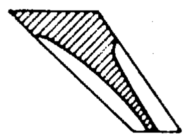	300	—	NONE			LOCKED	
SWS-3c 74	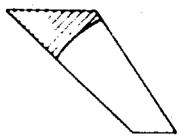	50.0	0.02	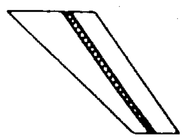	200	0.028	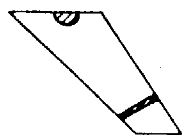	227	0.011	TORSION	300		74.4	

Table 5. Experimental vibration data. (cont.)

MODE / MODEL	FIRST			SECOND			THIRD			FOURTH			UNCOUPLED PITCH	
	f (cps)		g	f		g	f		g	f		g	f	g
SWS – 3d LOCKED	65 6	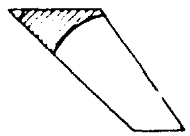	0.018	244	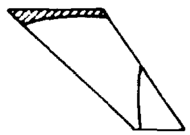	0.026	275	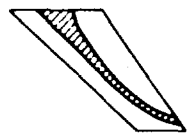	0.015		NONE		LOCKED	
SWS – 3d 87	54.1	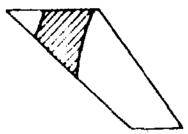	0 026	225	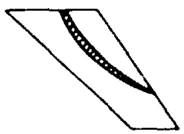	0.031	244	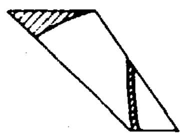	0.022	350	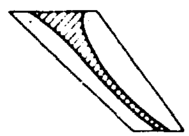	0.018	86.7	
SWS – 3e LOCKED	68	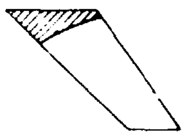	—	255	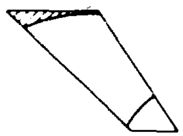	—	290	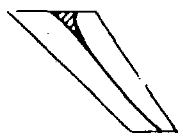	—		NONE		LOCKED	
SWS – 3e - 120	57 5	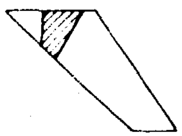	0.02	234	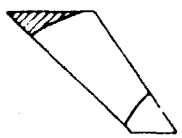	—	247	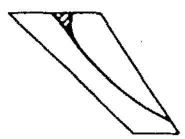	—		NONE		120	

Table 6. Experimental influence coefficient data.

SWS-1

Load \ Read	1	2	3	4	5	6	7	8	9
1	0.0314	0.0338	0.0359	0.0153	0.0192	0.0200	0.0050	0.0068	0.0084
2	0.0338	0.0366	0.0385	0.0163	0.0200	0.0168	0.0048	0.0090	0.0054
3	0.0359	0.0385	0.0318	0.0168	0.0203	0.0236	0.0051	0.0085	0.0153
4	0.0153	0.0163	0.0168	0.0088	0.0098	0.0095	0.0035	0.0043	0.0039
5	0.0192	0.0200	0.0203	0.0098	0.0118	0.0135	0.0033	0.0051	0.0067
6	0.0200	0.0168	0.0236	0.0095	0.0135	0.0176	0.0036	0.0057	0.0103
7	0.0050	0.0048	0.0051	0.0035	0.0033	0.0036	0.0015	0.0019	0.0022
8	0.0068	0.0090	0.0085	0.0043	0.0051	0.0057	0.0019	0.0040	0.0032
9	0.0084	0.0054	0.0153	0.0039	0.0067	0.0103	0.0022	0.0032	0.0002

SWS-1b-142

Load \ Read	1	2	3	4	5	6	7	8	9
1	0.0386	0.0412	0.0426	0.0168	0.0222	0.0270	0.0060	0.0087	0.0128
2	0.0406	0.0484	0.0508	0.0169	0.0248	0.0304	0.0061	0.0095	0.0146
3	0.0424	0.0512	0.0656	0.0178	0.0270	0.0343	0.0063	0.0104	0.0164
4	0.0190	0.0196	0.0206	0.0173	0.0115	0.0137	0.0042	0.0050	0.0072
5	0.0220	0.0248	0.0264	0.0108	0.0169	0.0187	0.0039	0.0063	0.0096
6	0.0254	0.0308	0.0338	0.0107	0.0182	0.0256	0.0041	0.0073	0.0120
7	0.0055	0.0059	0.0059	0.0026	0.0038	0.0039	0.0031	0.0017	0.0021
8	0.0087	0.0099	0.0106	0.0039	0.0067	0.0075	0.0019	0.0038	0.0045
9	0.0118	0.0146	0.0159	0.0051	0.0096	0.0120	0.0022	0.0043	0.0092

SWS-1-98

Load \ Read	1	2	3	4	5	6	7	8	9
1	0.0386	0.0428	0.0452	0.0188	0.0220	0.0272	0.0070	0.0102	0.0144
2	0.0428	0.0497	0.0533	0.0220	0.0260	0.0314	0.0082	0.0122	0.0174
3	0.0452	0.0533	0.0635	0.0212	0.0283	0.0346	0.0073	0.0133	0.0190
4	0.0188	0.0220	0.0212	0.0096	0.0122	0.0120	0.0043	0.0054	0.0072
5	0.0220	0.0260	0.0283	0.0122	0.0163	0.0189	0.0042	0.0080	0.0102
6	0.0272	0.0314	0.0346	0.0120	0.0189	0.0261	0.0035	0.0091	0.0154
7	0.0070	0.0082	0.0073	0.0043	0.0042	0.0035	0.0016	0.0017	0.0021
8	0.0102	0.0122	0.0133	0.0054	0.0080	0.0091	0.0017	0.0039	0.0051
9	0.0144	0.0174	0.0190	0.0072	0.0102	0.0154	0.0021	0.0051	0.0094

SWS-1c-48

Load \ Read	1	2	3	4	5	6	7	8	9
1	0.0570	0.0614	0.0684	0.0270	0.0356	0.0448	0.0057	0.0140	0.0240
2	0.0624	0.0714	0.0824	0.0300	0.0410	0.0528	0.0058	0.0163	0.0284
3	0.0688	0.0810	0.1028	0.0334	0.0460	0.0610	0.0058	0.0182	0.0332
4	0.0276	0.0298	0.0332	0.0165	0.0189	0.0233	0.0035	0.0076	0.0124
5	0.0360	0.0410	0.0460	0.0189	0.0291	0.0330	0.0036	0.0105	0.0181
6	0.0438	0.0514	0.0594	0.0226	0.0317	0.0446	0.0040	0.0126	0.0236
7	0.0051	0.0050	0.0053	0.0030	0.0032	0.0035	0.0019	0.0012	0.0015
8	0.0147	0.0162	0.0185	0.0077	0.0103	0.0137	0.0015	0.0048	0.0083
9	0.0244	0.0280	0.0327	0.0124	0.0179	0.0242	0.0017	0.0075	0.0169

SWS-1-138

Load \ Read	1	2	3	4	5	6	7	8	9
1	0.0412	0.0423	0.0458	0.0213	0.0250	0.0288	0.0078	0.0113	0.0144
2	0.0423	0.0462	0.0527	0.0255	0.0262	0.0358	0.0075	0.0121	0.0155
3	0.0458	0.0527	0.0635	0.0236	0.0295	0.0305	0.0102	0.0146	0.0160
4	0.0213	0.0255	0.0236	0.0137	0.0160	0.0162	0.0061	0.0072	0.0084
5	0.0250	0.0262	0.0295	0.0160	0.0173	0.0203	0.0070	0.0080	0.0107
6	0.0288	0.0358	0.0305	0.0162	0.0203	0.0260	0.0059	0.0098	0.0145
7	0.0078	0.0075	0.0102	0.0061	0.0070	0.0059	0.0033	0.0056	0.0033
8	0.0113	0.0121	0.0146	0.0072	0.0080	0.0098	0.0056	0.0042	0.0058
9	0.0144	0.0155	0.0160	0.0084	0.0107	0.0145	0.0033	0.0058	0.0092

SWS-1e-74

Load \ Read	1	2	3	4	5	6	7	8	9
1	0.0428	0.0460	0.0492	0.0188	0.0246	0.0312	0.0022	0.0080	0.0126
2	0.0456	0.0534	0.0592	0.0208	0.0274	0.0368	0.0022	0.0116	0.0162
3	0.0500	0.0598	0.0756	0.0202	0.0314	0.0400	0.0024	0.0118	0.0402
4	0.0194	0.0212	0.0220	0.0102	0.0112	0.0128	0.0004	0.0042	0.0070
5	0.0254	0.0484	0.0316	0.0128	0.0202	0.0202	0.0008	0.0044	0.0094
6	0.0294	0.0356	0.0408	0.0150	0.0210	0.0536	0.0006	0.0072	0.0122
7	0.0035	0.0033	0.0035	0.0014	0.0012	0.0011	0.0016	0.0005	0.0005
8	0.0092	0.0109	0.0114	0.0642	0.0062	0.0072	0.0003	0.0023	0.0042
9	0.0146	0.0175	0.0202	0.0066	0.0110	0.0139	0	0.0044	0.0111

Table 6. Experimental influence coefficient data (cont.)

SWS-2

Load \ Read	1	2	3	4	5	6	7	8	9
1	0.0430	0.0430	0.0446	0.0196	0.0212	0.0254	0.0048	0.0075	0.0103
2	0.0438	0.0502	0.0546	0.0196	0.0244	0.0308	0.0051	0.0085	0.0129
3	0.0464	0.0562	0.0716	0.0200	0.0272	0.0368	0.0052	0.0088	0.0140
4	0.0188	0.0192	0.0194	0.0124	0.0116	0.0118	0.0030	0.0044	0.0047
5	0.0222	0.0244	0.0266	0.0116	0.0158	0.0172	0.0032	0.0052	0.0078
6	0.0252	0.0300	0.0346	0.0120	0.0168	0.0260	0.0029	0.0061	0.0104
7	0.0048	0.0051	0.0052	0.0030	0.0032	0.0029	0.0028	0.0014	0.0012
8	0.0075	0.0085	0.0088	0.0044	0.0052	0.0061	0.0014	0.0030	0.0035
9	0.0103	0.0119	0.0140	0.0047	0.0078	0.0104	0.0012	0.0035	0.0013

SWS-3b-53

Load \ Read	1	2	3	4	5	6	7	8	9
1	0.0460	0.0568	0.0614	0.0240	0.0345	0.0422	0.0048	0.0130	0.0220
2	0.0598	0.0762	0.0790	0.0287	0.0387	0.0507	0.0036	0.0151	0.0264
3	0.0678	0.0776	0.0978	0.0318	0.0441	0.0591	0.0038	0.0193	0.0307
4	0.0243	0.0276	0.0314	0.0154	0.0174	0.0204	0.0027	0.0074	0.0105
5	0.0343	0.0361	0.0436	0.0180	0.0258	0.0299	0.0029	0.0105	0.0163
6	0.0436	0.0499	0.0576	0.0219	0.0310	0.0421	0.0062	0.0105	0.0220
7	0.0044	0.0037	0.0038	0.0028	0.0022	0.0025	0.0020	0.0016	0.0010
8	0.0135	0.0148	0.0170	0.0075	0.0085	0.0121	0.0014	0.0046	0.0071
9	0.0232	0.0266	0.0305	0.0126	0.0173	0.0276	0.0012	0.0075	0.0163

SWS-3-53

Load \ Read	1	2	3	4	5	6	7	8	9
1	0.0440	0.0540	0.0588	0.0212	0.0300	0.0388	0	0.0104	0.0206
2	0.0526	0.0638	0.0716	0.0242	0.0354	0.0448	0.0002	0.0134	0.0254
3	0.0582	0.0720	0.0906	0.0270	0.0404	0.0532	0.0002	0.0104	0.0290
4	0.0218	0.0244	0.0266	0.0190	0.0142	0.0192	0	0.0046	0.0094
5	0.0278	0.0352	0.0378	0.0144	0.0240	0.0276	0	0.0082	0.0154
6	0.0370	0.0434	0.0524	0.0184	0.0274	0.0390	0	0.0108	0.0208
7	0.0027	0.0023	0.0035	0.0013	0.0016	0.0006	0.0002	0.0010	0
8	0.0110	0.0131	0.0154	0.0049	0.0084	0.0103	0	0.0051	0.0061
9	0.0199	0.0231	0.0272	0.0078	0.0156	0.0199	0	0.0060	0.0142

SWS-3d-87*

Load \ Read	1	2	3	4	5	6	7	8	9
1	0.0424	0.0468	0.0468	0.0232	0.0248	0.0320	0.0060	0.0116	0.0274
2	0.0468	0.0540	0.0628	0.0240	0.0288	0.0372	0.0072	0.0126	0.0180
3	0.0468	0.0628	0.0780	0.0252	0.0316	0.0420	0.0072	0.0132	0.0202
4	0.0232	0.0240	0.0252	0.0156	0.0152	0.0082	0.0054	0.0074	0.0096
5	0.0248	0.0288	0.0316	0.0152	0.0218	0.0110	0.0052	0.0086	0.0116
6	0.0320	0.0372	0.0420	0.0082	0.0110	0.0150	0.0050	0.0098	0.0148
7	0.0060	0.0072	0.0072	0.0054	0.0052	0.0050	0.0041	0.0027	0.0026
8	0.0116	0.0126	0.0132	0.0074	0.0086	0.0098	0.0027	0.0056	0.0061
9	0.0274	0.0180	0.0202	0.0096	0.0116	0.0148	0.0026	0.0061	0.0121

SWS-3a-63

Load \ Read	1	2	3	4	5	6	7	8	9
1	0.0444	0.0480	0.0529	0.0206	0.0265	0.0328	0.0038	0.0104	0.0161
2	0.0480	0.0594	0.0646	0.0229	0.0309	0.0397	0.0038	0.0118	0.0198
3	0.0529	0.0646	0.0796	0.0247	0.0338	0.0451	0.0033	0.0129	0.0226
4	0.0206	0.0229	0.0247	0.0130	0.0138	0.0163	0.0025	0.0058	0.0084
5	0.0265	0.0309	0.0338	0.0138	0.0217	0.0234	0.0022	0.0073	0.0122
6	0.0328	0.0397	0.0451	0.0163	0.0234	0.0325	0.0022	0.0086	0.0160
7	0.0038	0.0038	0.0033	0.0025	0.0022	0.0022	0.0035	0.0012	0.0014
8	0.0104	0.0118	0.0129	0.0058	0.0073	0.0086	0.0012	0.0052	0.0055
9	0.0161	0.0198	0.0226	0.0084	0.0122	0.0160	0.0014	0.0053	0.0122

* Matrix assumed symmetric for this model.